Airplane cabin mixing ventilation with time-periodic supply

Received: 11 May 2022 | Revised: 9 October 2022 | Accepted: 10 October 2022

DOI: 10.1111/ina.13151

ORIGINAL ARTICLE

WILEY

Airplane cabin mixing ventilation with time-periodic supply: Contaminant mass fluxes and ventilation efficiency

Jo-Hendrik Thysen[1] | Twan van Hooff[2] | Bert Blocken[1,2] | GertJan van Heijst[3]

[1]Building Physics and Sustainable Design, Department of Civil Engineering, KU Leuven, Leuven, Belgium

[2]Building Physics and Services, Department of the Built Environment, Eindhoven University of Technology, Eindhoven, The Netherlands

[3]Fluids and Flows, Department of Applied Physics, Eindhoven University of Technology, Eindhoven, The Netherlands

Correspondence
Jo-Hendrik Thysen, Building Physics and Sustainable Design, Department of Civil Engineering, KU Leuven, Kasteelpark Arenberg 40 – bus 2447, 3001 Leuven, Belgium.
Email: johendrik.thysen@kuleuven.be

Funding information
Fonds Wetenschappelijk Onderzoek

Abstract

Airplane cabin ventilation is essential to ensure passengers' well-being. The conventional ventilation method is mixing ventilation with a statistically steady supply, which, according to former studies, has reached its limits regarding, for example, the ventilation efficiency. However, the effect of a statistically unsteady (time-periodic) supply on the mixing ventilation efficiency has remained largely unexplored. This research uses computational fluid dynamics (CFD) with the large eddy simulation (LES) approach to study isothermal time-periodic mixing ventilation in a section of a single-aisle airplane cabin model, in which the air exhaled by the passengers functions as (passive) contaminants. Two time-periodic supply strategies are evaluated. The induced time-periodic airflow patterns promote an efficient delivery of fresh air to the passenger zone and affect the passengers' expiratory plumes. This results in increased mean contaminant mass fluxes, causing a strong reduction of the mean contaminant concentrations in the passenger zone (up to 23%) and an increased contaminant extraction from the cabin. Mean velocities increase with up to 55% but remain within the comfortable range. It is shown that the ventilation efficiency improves; that is, the contaminant removal effectiveness and air change efficiency (in the full cabin volume) increase with up to 20% and 7%, respectively.

KEYWORDS
airplane cabin, computational fluid dynamics (CFD), convective and turbulent contaminant mass fluxes, large eddy simulation (LES), time-periodic mixing ventilation, ventilation efficiency

1 | INTRODUCTION

Ventilation of airplane cabins is indispensable to the realization of a healthy and comfortable cabin environment[1,2] for the annual 4.5 billion passengers worldwide (in 2019).[3] Managed by the environmental control system (ECS), the ventilation (fresh) air should provide a reduction of airborne contaminants (e.g., ozone, volatile organic compounds, CO_2, bioaerosols potentially including influenza or SARS viruses[2,4]) and control the air temperature. The thereby induced airflow patterns should operate as such, with maximum dilution and extraction of contaminants and without the introduction of uncomfortable draft. Besides, pressurization of the cabin is also realized by the ventilation air. Since the ventilation air is drawn from the jet engines and requires conditioning,[2] it is energy consuming and expensive[5–8] while both energy use and costs are preferably limited to a minimum.

The main air distribution in airplane cabins is most commonly provided through overhead (ceiling and/or lateral) diffusers supplying high-momentum air with air extraction at floor level,[4] also called mixing ventilation (MV). Many experimental and computational fluid dynamics (CFD) papers[9–32] can be found in the literature in which the MV flow in different airplane cabin configurations (e.g., single-aisle as the B737-200, A320, and MD-82, or twin-aisle as the B767-300 or A380) was investigated and characterized in terms of its mean and instantaneous flow patterns, distributions of velocity, turbulence, temperature, relative humidity, pressure, and vorticity. The ventilation performance regarding the distribution of (gaseous) contaminants,[11,13,15,17,28,29,32,33–37] droplet and aerosol deposition/dispersion,[15,32,38–45] age of air,[13,27,46,47] thermal comfort (predicted mean vote, predicted percentage dissatisfied)[47–49] and heat[27,48,50] or contaminant[13,35] removal was also reported.

In MV, circulation patterns[51] and high turbulence intensities[16,19] are induced in order to mix (dilute) the cabin air, which should create a homogeneous air distribution with relatively uniform temperature and contaminant levels[19,52,53] and low velocities.[16,19,53] However, concerns about the air dilution in MV are manifold. Typically, this causes an air (ex)change efficiency (ACE)[54] below the value of 0.5. Also, contaminants may be dispersed throughout the cabin,[21,35,44] mainly in the lateral direction (cross contamination)[34,40] due to full-length inlet/outlet slots[55,56] designed to limit the longitudinal flow (although longitudinal transport can still be present[20,33,34,40,44]), resulting in a contaminant removal effectiveness (CRE)[13,35] of usually less than unity. A uniform temperature distribution, although it enhances thermal comfort, causes the theoretical upper limit of the heat removal efficiency (HRE)[48] to be limited to 0.5. Furthermore, stagnant zones may be present giving rise to contaminant/heat lock up[13,25,27,36,45,57] and the high-momentum supply air may cause thermal discomfort.[48,49,58] Some studies[36,37,40] pointed out that an improved air quality may be obtained by increasing the ventilation flow rate, though at the expense of increased energy use.

In order to counteract the potential deficiencies of MV, alternative main ventilation methods were studied. In displacement ventilation (DV), air is usually supplied at floor level via diffusers at the sides,[27,59,60] below the seats[48,61] or under the aisle,[35,46,52,62,63] while being extracted above the passengers, in order to displace the cabin air rather than to dilute it. DV can therefore yield higher values of the ACE,[54] CRE[27,60] and HRE[27,48,59–61] (yielding opportunities for energy savings[27,48,61]) compared to MV, but may be more susceptible to temperature stratification[27,48,52,59–61] and draft at foot level[48,51,58] potentially causing thermal discomfort. Some studies reported the thermally stratified flow to cause contaminant/heat accumulation right above the breathing zone,[4,8,63] and insufficient cooling under hot ambient conditions (before take-off or after landing).[46] In addition, DV relies on the presence/distribution of heat sources, and it is also less suitable for heating.[61]

Other proposed ventilation methods are in essence modified versions of traditional MV and DV, or are a combination of both.[27,46,48,50,58,59] Furthermore, some studies proposed personal ventilation (PV) methods complementary to the main air distribution, for example, using overhead gaspers that may improve thermal comfort[42,64] or may help in contaminant reduction.[65–68] This is particularly true for the more advanced PV methods that incorporate a direct supply and/or extraction of air in the passengers' microenvironment,[8,35,52,69–73] for example, through seat-mounted supply and extraction devices.

Rather than resorting to other ventilation methods, which can be difficult to implement in (existing) cabins due to high costs[70] or restrictions by the (aesthetic) interior design,[47,51] this paper investigates whether MV can be optimized via modifications to the supplied air, since its momentum is the main driver of the air distribution.[57] Whereas in all conventional cabin ventilation methods, air is supplied at a constant (statistically steady) rate, the focus here is on the application of time-periodically varying supply flow rates. Wu and Ahmed[74,75] showed with unsteady Reynolds-averaged Navier–Stokes (RANS) CFD simulations in a twin-aisle cabin, that time-periodic supply flow rates improved the MV performance compared to statistically steady ventilation (i.e., lower air temperatures, concentration levels and mean age of air). Due to the supply jets being directed toward the passenger zone, by switching between (constant) high and low flow rates (square-wave signal), an oscillatory interaction between the supply jets and the passengers' thermal plumes was generated and maintained. Another time-periodic supply strategy is the continuous varying of the supply flow rate (sine-wave signal), which in essence can be regarded as a more active forcing of the flow patterns compared with this of Wu and Ahmed.[74,75] Kandzia et al.,[76] Schmidt et al.,[77] and van Hooff and Blocken[78] investigated such inlet condition in generic opposing-jet MV flow configurations that resemble those often encountered in cabin ventilation (in which the supply jets coming from both sides interact above the aisle). They showed that large-scale eddies can break up[76,77] and contaminant

Practical implications

- Time-periodic mixing ventilation strongly reduces the mean penetration of the passengers' expiratory plumes to the passengers in front (longitudinal transport), which may protect them from being exposed to high contaminant concentration levels.
- Whereas longitudinal (mean) contaminant mass transport reduces, the mass fluxes (both convective and turbulent) in the vertical cross-section of the cabin increase, with convective transport remaining the dominant mechanism.
- The two evaluated time-periodic supply strategies affect the mean mass fluxes and hence the mean concentration levels at every passenger seat differently: the lowest/highest mean concentrations are observed at the window/middle seat (statistically steady supply), aisle/middle seat (asymmetric time-periodic supply), and window/aisle seat (symmetric time-periodic supply).
- The asymmetric time-periodic supply strategy shows the best ventilation efficiency.
- Overall, time-periodic mixing ventilation shows the potential for improved cabin air quality compared to a conventional statistically steady supply, although the realization of optimal indoor conditions (including thermal comfort) will require careful selection of the supply parameters.

concentrations in stagnant zones were reduced while an increased CRE was achieved.[78] Other studies showing improved mixing under time-periodic inlet conditions can be found in, for example, Thysen et al.[79] However, to the best of our knowledge, a continuous time-periodically varying (sine-wave) supply flow rate has not yet been examined for airplane cabin ventilation.

Therefore, this paper presents large eddy simulations (LES) of airplane (opposing-jet) MV with time-periodic supply flow rates according to a sine wave with a relatively short period of the order of seconds. Distributions of the mean velocity and (passive gaseous) contaminant concentration are analyzed and compared with those obtained in the conventional statistically steady ventilation (SV) case. The performance of time-periodic ventilation (TPV) is assessed from the ACE and CRE, and insights into the mean concentration distribution are obtained from the inspection of mass fluxes that are responsible for the contaminant transport. It should be mentioned that thermal effects from heat sources (e.g., passenger thermal plumes) are not implemented (isothermal conditions). This choice is substantiated by previous studies[19,21,29,57] that showed thermal effects to be of secondary importance compared with the significant impact of the supply jets in opposing-jet SV configurations. Thermal effects may create a more stable flow and have an influence on the mean flow symmetry to some degree. In addition, an increased width of the supply jets (i.e., more entrainment), an increased overall flow velocity, and a higher turbulent kinetic energy of the smaller-scale flow structures were also observed under non-isothermal conditions,[19,21,22,25,29] although the prevailing flow patterns remained dominated by the high-momentum opposing supply jets.

The structure of the paper is as follows. Section 2 outlines the computational parameters of the LES simulations, after which Section 3 presents a brief description of the contaminant transport equations and performance indicators. In Section 4, the computational results of the SV versus TPV cases are outlined, followed by Section 5 which provides the discussion, limitations, and suggestions for future work. The conclusions are summarized in Section 6.

2 | COMPUTATIONAL PARAMETERS

2.1 | Computational domain

The computational geometry, shown in Figure 1, is constructed in SpaceClaim 2020 R2[80] and represents a section of a single-aisle airplane cabin similar to, for example, the Airbus A320 or Boeing 737–200 series.[81,82] The cabin width (W) at floor level measures 3.31 m (maximum width is 3.54 m) and the height (H) is 2.20 m (width-to-height ratio is ≈ 1.5) (Figure 1A). The section consists of three (identical) rows corresponding to 18 passenger seats with a seat pitch (S) of 0.80 m,[57,83] resulting in a cabin section length (L) of 2.40 m. The overhead stowage compartments (OHSCs), placed 1.59 m above the floor, have the shape of traditional pushing-up type bins[47] with a spacing in between of 1.16 m (Figure 1B).

Fresh air is supplied to the cabin through the opposing ceiling inlets at the top of the cabin and the opposing lateral inlets located directly below the OHSCs. They are modeled as fully open linear slots (Figure 1C), that is, without any specific diffuser geometry such as a honeycomb structure and/or a multi-slot configuration.[16,21,24,57] The inlet slot dimensions are 25 × 731.5 mm^2 with a separation distance between adjacent slots of 68.5 mm (Cao et al.[57]). The dimensions of the outlet slots at floor level, through which air exits the cabin, are the same except for the slot height which is now 50 mm.

The seat geometry is slightly simplified to allow for an easier generation of the computational grid (e.g., gaps between individual seats are omitted), although their general shape and dimensions are in line with those reported in the B737 documentation[82] and the guidelines provided by Quigley et al.[83] Specific seat dimensions are indicated in Figure 1B. The seats are positioned such that the middle of the seat cushion is aligned with the middle of the row. The horizontal distance between the seats of subsequent rows is approximately 0.20 m and the distance between the seats on the left and right side (aisle) is 0.51 m.

The passenger model is created in Meshmixer.[84] The height of a seated passenger is 1.32 m and its total body surface is 1.64 m^2.

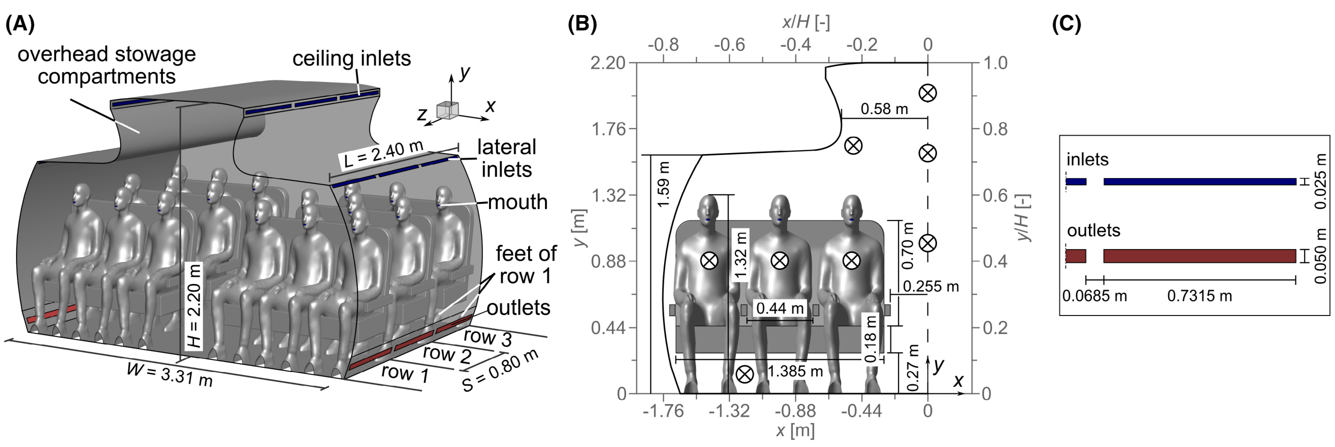

FIGURE 1 3D computational geometry of airplane cabin and passengers. (A) Perspective view. (B) Front view with indication of monitoring points (circles) located in vertical midplane $z/H \approx 0.55$. (C) Dimensions of inlets and outlets and spacing between two adjacent inlets/outlets

At the mouth of each passenger, a small opening with an area of approximately 400 mm^2 is incorporated through which exhaled air is introduced into the cabin (creating so-called expiratory plumes). Note that the feet of the passengers at the first row are cut and moved behind the seats of row three.

2.2 | Computational grid

Figure 2 shows the high-resolution computational hybrid grid constructed with ANSYS Fluent meshing 2020 R2,[85] which consists of a non-conformal hexahedral grid in the bulk of the domain (cubical cells with size change 1:2) and hexagonal prism layers along the boundaries, with in between polyhedral cells to make the transition between the bulk flow and the boundary layer. This grid type is chosen instead of the tetrahedral grids commonly used in airplane ventilation studies, since, ideally, cubical cells are used for LES,[86] which can provide a higher accuracy as well.[87–89] The use of prism layers to resolve the viscous sublayer is common practice for meshing complex boundaries and it provides a higher grid quality than with tetrahedral cells.[90,91] Furthermore, polyhedral cells have the advantage of being less sensitive to stretching compared to tetrahedral cells (skewness) and perform better in resolving gradients of flow variables due to every polyhedral cell having many neighboring cells.[92–94]

The total cell count is 30 538 995. The length of the cells in the cubical part of the grid (bulk flow) varies from 2.3 to 18.3 mm, which is in the same range as in other airplane ventilation CFD studies.[18,23,95] Within the interaction zones of the opposing lateral and ceiling jets the cell length equals 18.3 and 4.6 mm, respectively, in line with the length scale to be used in LES within these zones according to Wang et al.[26] The number of prism layers used in the boundary layer grid is 10, with the height of the first prism cell layer equal to 0.5 mm. The growth rate of the prism layers is determined locally (last ratio method[91]), by setting the last cell layer height to 40% of the local surface cell length, with the cell layers in between the first and last cell layers growing exponentially. The dimensionless wall unit $y^* < 0.45$ in all simulations. All inlets have 20 cells over the inlet height.

The current grid resolution is the result of several preliminary simulations in which the grid was systematically refined to ensure that the value of the ratio of the mean resolved to the mean total turbulent kinetic energy (K_{res}/K) would be larger than 80%, which is a measure of well-resolved LES.[86] Figure 3A,B shows K_{res}/K obtained along profiles in the vertical midplane ($z/H \approx 0.55$; Figure 2) and horizontal plane ($y/H \approx 0.53$), respectively, for case SV. The results in Figure 3A are only shown in half the domain ($x/H < 0$) and in Figure 3B for row two ($0.36 < z/H < 0.73$) because of the mean flow being close to symmetric. The dashed lines indicate the sampling locations. It is clear that K_{res}/K is larger than 80% (average of all sampling lines is 93%).

2.3 | Boundary conditions

Three ventilation cases with different inlet conditions are simulated, with case one representing conventional SV, and cases two and three TPV strategies. The inlet velocities u_0 in each of the cases evolve over time t according to:

$$u_0(t) / U_{0,SV} = 1 + \left(\Delta U_0 / U_{0,SV}\right) \cdot \sin\left[2\pi t / T + \varphi\right] + u_0'(t) / U_{0,SV} \quad (1)$$

$U_{0,SV} = 0.771$ m/s is the constant contribution to u_0, ΔU_0 the amplitude of the sinusoidal contribution with period T and phase angle φ, and u_0' representing turbulent fluctuations. The inlet velocities during one supply cycle (1 T) in the SV and two TPV cases are shown at the top of Figures 4 and 5 and 6, respectively, with below several snapshots of the flow field that will be discussed

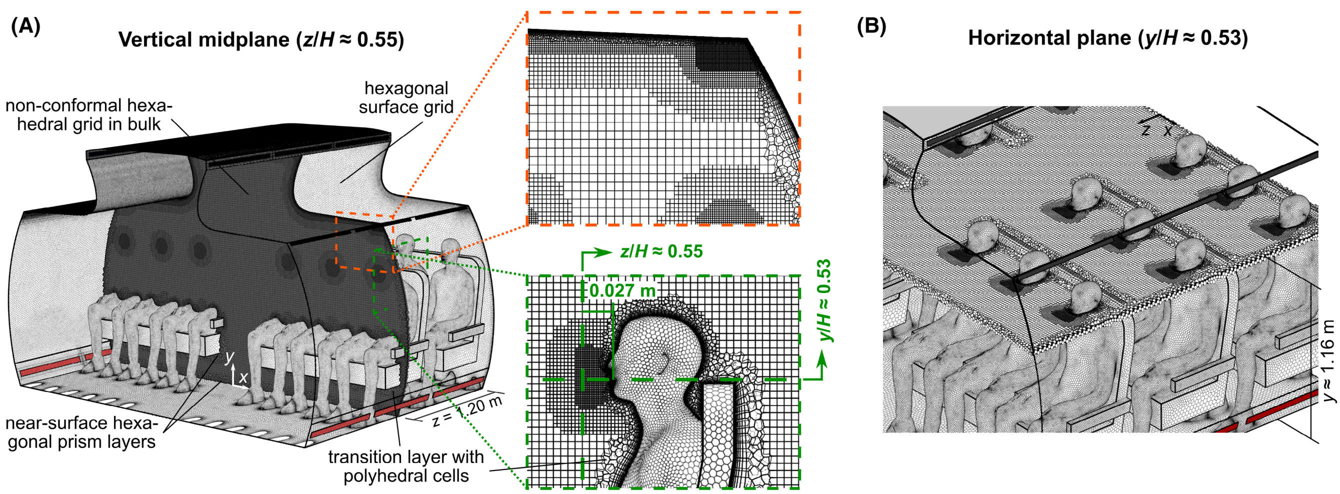

FIGURE 2 Computational grid (30 538 995 cells) in several planes: (A) vertical midplane ($z/H \approx 0.55$) with zoom-in on area at inlet and passenger, and (B) horizontal plane intersecting passengers' mouths ($y/H \approx 0.53$). Note that in (A) passengers in row 1 are omitted for better visibility

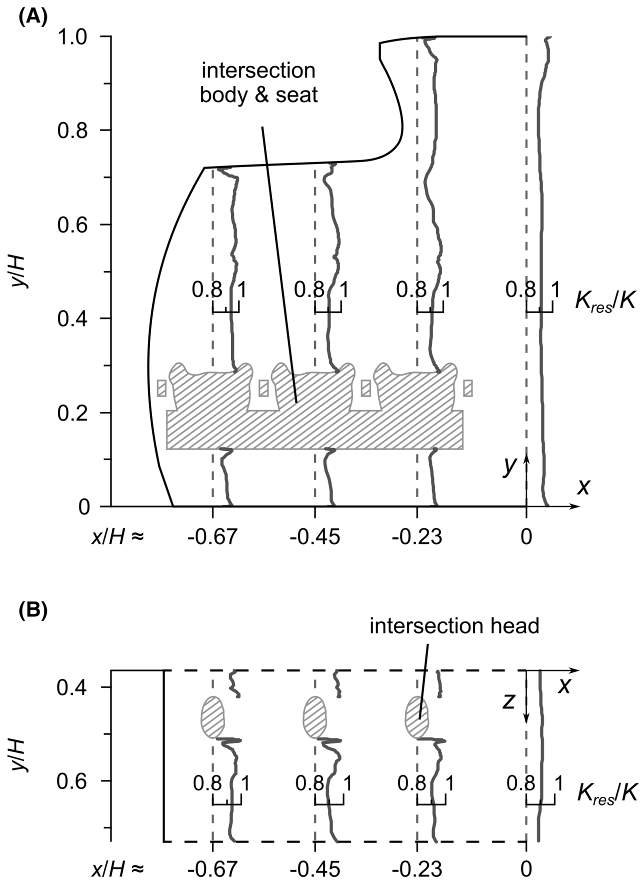

FIGURE 3 Profiles of ratio of mean resolved to mean total turbulent kinetic energy (K_{res}/K) in case SV: (A) vertical midplane ($z/H \approx 0.55$) and (B) horizontal plane ($y/H \approx 0.53$)

later. Note that the contribution of u_0' is not visualized for the sake of clarity. In case SV (top of Figure 4), $\Delta U_0 = 0$ and the statistically steady inlet velocity at *all* ceiling/lateral inlets equals $U_{0,SV}$, according to a constant total volume supply flow rate of 9.4 L/s per passenger.[2] The inlet velocities in the two TPV cases (top of Figures 5 and 6) include a sinusoidal contribution with $\Delta U_0/U_{0,SV} = 1$ and $T = 1T_{FT}$, where T_{FT} is the flow-through time ≈9.9 s as calculated from the circumference of half the domain and $U_{0,SV}$. The difference between both TPV cases is φ at each inlet: in the case denoted as "TPV_AS" (Figure 5), u_0 of all ceiling and lateral inlets at the same side (left *or* right) of the cabin is equal, but $\varphi = 180°$ out of phase with respect to the opposing side, whereas in the case hereafter called "TPV_SS" (Figure 6), u_0 of all lateral inlets (left *and* right side) is equal, but $\varphi = 180°$ out of phase with respect to all ceiling inlets. This means that in TPV_AS the supply flow rate at both sides is time-periodically "asymmetric" with respect to the vertical symmetry plane ($x/H = 0$; Figure 1B) whereas in TPV_SS, "symmetric" supply flow rates are used. Note that in all three ventilation cases, the total supply flow rate remains unchanged over time (9.4 L/s per passenger).

The turbulent velocity fluctuations at the inlet (u_0') are generated via the vortex method.[96] The inlet turbulence intensity is set to 30%[26] and the hydraulic diameter is ≈0.0483 m. Also, the inlet subgrid-scale (SGS) kinetic energy is prescribed to be ≈0.0161 m^2/s^2, which equals 20% of the total inlet turbulent kinetic energy[86] (determined from the specified turbulence intensity[97]). Isothermal conditions are considered; hence, no heat sources are present in the cabin (i.e., no heat load induced by the passengers, and equal density of the supply air and cabin air). In addition, no contaminants are present in the supply air.

The air exhaled by each passenger is modeled using the following settings. Through the mouths of the passengers, air is supplied with a constant velocity of 0.349 m/s perpendicular to the mouth surface, resulting in a volume flow rate of 8.4 L/min per passenger, which is the minute volume exhaled by a seated passenger.[98] The vortex method is used here as well to induce velocity fluctuations, with the turbulence intensity equal to 0.5%.[98] The hydraulic diameter of a mouth opening is ≈0.0196 m and the SGS kinetic energy is ≈$9{\cdot}10^{-7}$ m^2/s^2. The exhaled air is modeled as a passive gas (i.e., same density as supply and cabin air), whose transport is described by an Eulerian advection–diffusion equation (see Section 3). The exhaled air is regarded as the (constant) source of contaminant concentration (with exhaust rate G_c in kg/s). It does not interact (e.g., adsorption) with the cabin environment, nor undergoes (chemical) reactions.

The cabin outlets have zero static gauge pressure and on all surfaces the no-slip condition is applied, apart from the back and front planes ($z/H \approx 0$ and $z/H = 1.09$, respectively), which are set as periodic boundaries.

2.4 | Numerical procedure and settings

The LES of case SV is initialized with a steady RANS simulation (Renormalisation group[99] k-ε model) on which synthetic turbulence is superimposed.[100] Then, the LES start-up and time-averaging phases are performed. The start-up phase is conducted over four T_{FT}, with the first $0.5T_{FT}$ carried out using the iterative time-advancement (ITA) scheme and the SIMPLEC algorithm for the pressure–velocity coupling,[85] together with increased under-relaxation factors (URFs) for pressure and momentum (0.9) for faster convergence.[100] A time step size of 0.001 s (≈$1.01{\cdot}10^{-4}T_{FT}$) and 10 iterations per time step allowed the residuals to decrease two to five orders of magnitude to values below 10^{-3}–10^{-7} in every time step. The time step size corresponds to a maximum Courant number of ≈5.2 (average Courant of ≈0.018). The remainder of the start-up phase ($3.5T_{FT}$) is performed with the non-ITA (NITA) scheme combined with the fractional-step method for pressure–velocity coupling to shorten the simulation time per time step, while the URFs are decreased to 0.7. For the TPV simulations, case SV after completion of its start-up phase is used as initial flow field. The NITA scheme, fractional-step method, and values of the URF are maintained. The start-up phase comprises three T_{FT} (equal to three periods of the inlet velocity). All simulation cases have a time-averaging phase encompassing $28T_{FT}$ (≈4.6 min), which is sufficiently long to achieve a converged mean solution. Similarly as outlined in Thysen et al.,[97] convergence is carefully checked from the ratio of the variation of the moving average of different flow

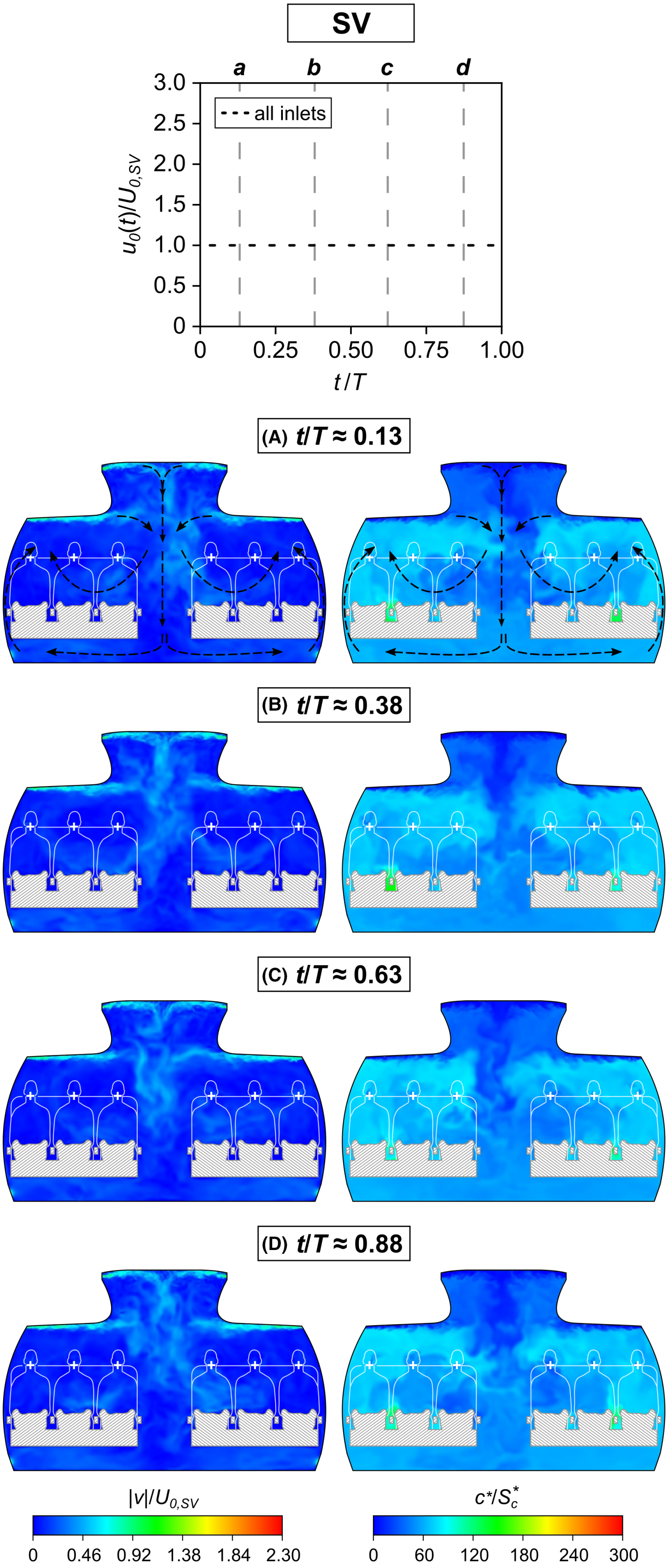

FIGURE 4 Dimensionless inlet velocity ($u_0(t)/U_{0,SV}$) (top) and contours of dimensionless instantaneous velocity magnitude ($|v|/U_{0,SV}$) (left) and dimensionless background concentration (c^*/S_c^*) (right) in vertical midplane ($z/H \approx 0.55$) at indicated instances *a-d* in case SV. Note that the exhaled air jets (with concentration c and source rate S_c) do not contribute to c^*

FIGURE 5 Dimensionless inlet velocity ($u_0(t)/U_{0,SV}$) (top) and contours of dimensionless instantaneous velocity magnitude ($|v|/U_{0,SV}$) (left) and dimensionless background concentration (c^*/S_c^*) (right) in vertical midplane ($z/H \approx 0.55$) at indicated instances *a-d* in case TPV_AS. Note that the exhaled air jets (with concentration *c* and source rate S_c) do not contribute to c^*

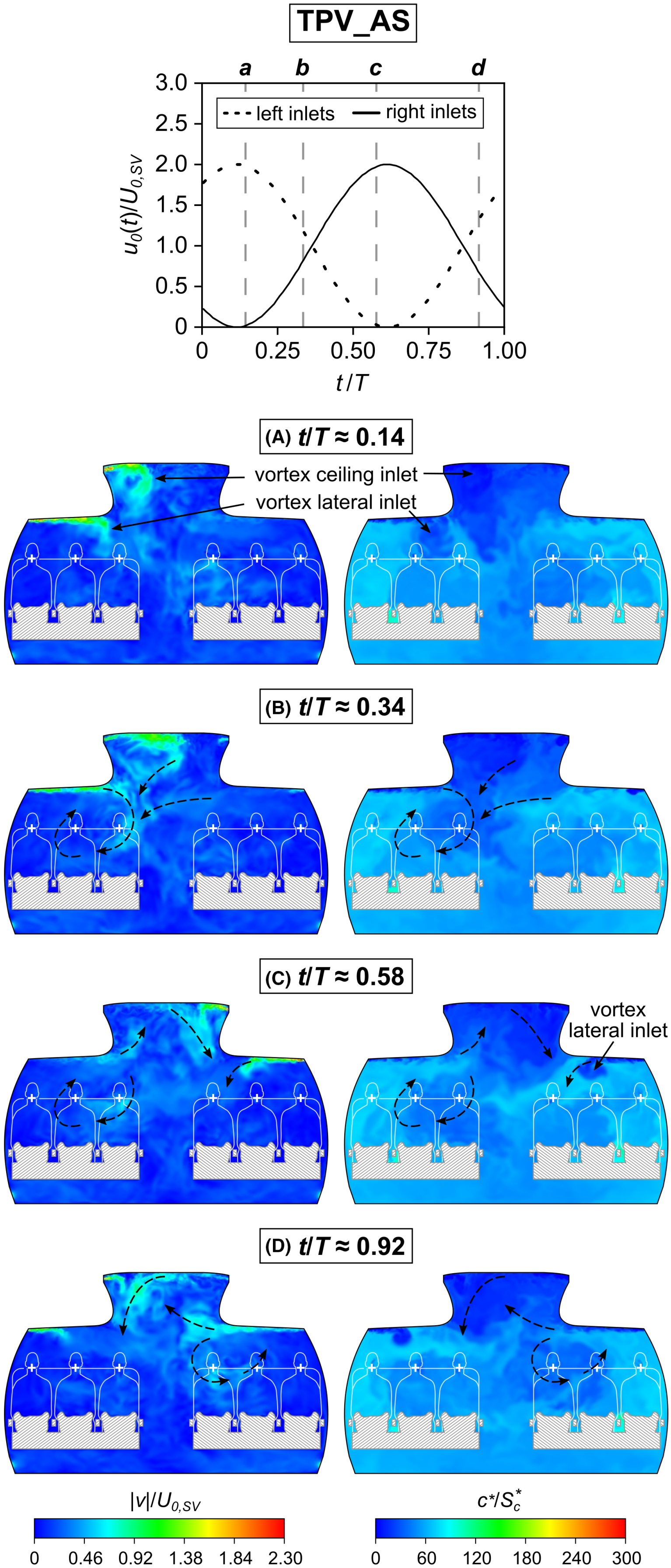

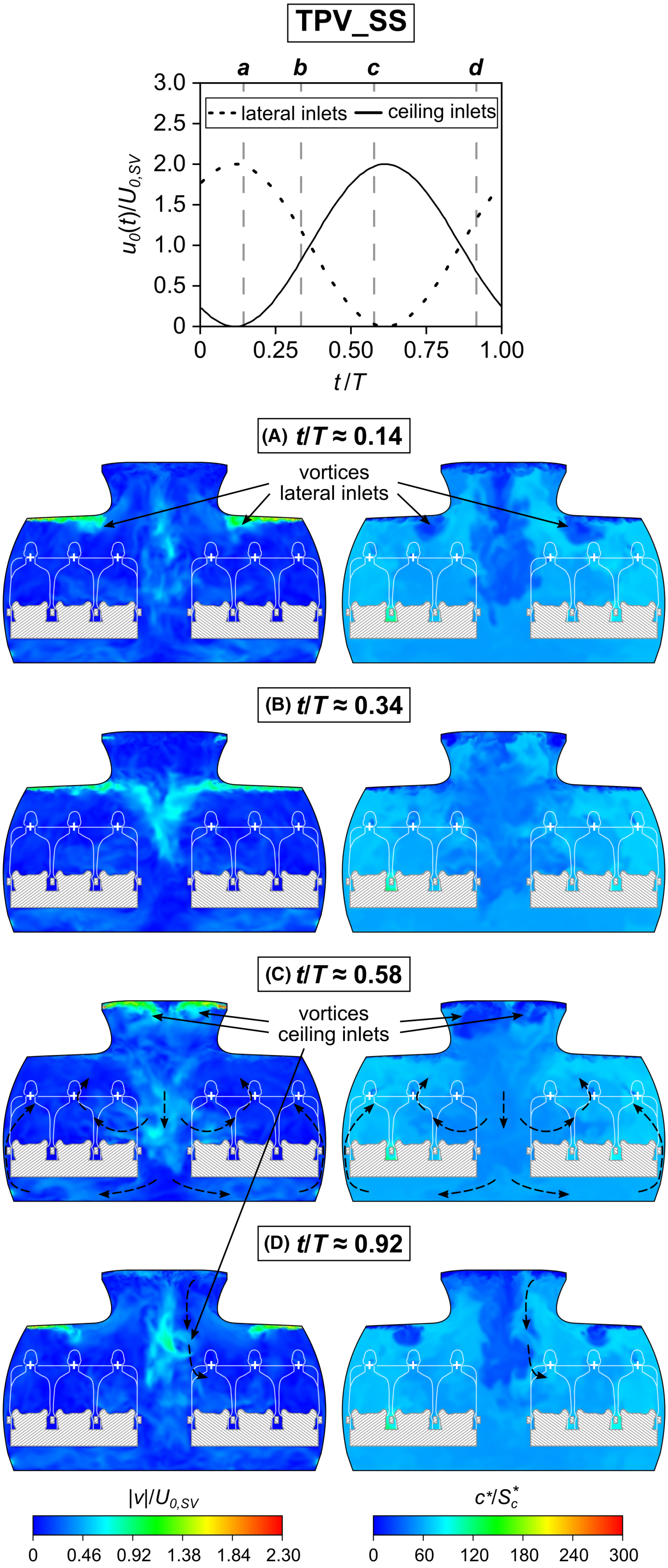

FIGURE 6 Dimensionless inlet velocity ($u_0(t)/U_{0,SV}$) (top) and contours of dimensionless instantaneous velocity magnitude ($|v|/U_{0,SV}$) (left) and dimensionless background concentration (c^*/S_c^*) (right) in vertical midplane ($z/H \approx 0.55$) at indicated instances *a*-*d* in case TPV_SS. Note that the exhaled air jets (with concentration *c* and source rate S_c) do not contribute to c^*

variables (recorded at several monitoring points shown in Figure 1B) to its corresponding final mean value, which decreases to values well below 1.9% (for velocity; apart from the two points within the jet interaction zone in TPV_AS at which 6.6% is noted) and 1.7% (concentration) at the end of the averaging phase.

In all simulations, discretization of momentum is governed by the bounded central differencing scheme, scalar variables are second order and time discretization uses the bounded second-order implicit scheme. For the gradients, the least-squares cell-based method is applied and the warped-face gradient correction is enabled for improved gradient accuracy (recommended for hybrid grids[91]). The total calculation time amounts approximately 38–44 days per simulation, using 512 cores (four nodes of 2×64-core 2.6 GHz AMD Rome 7H12 CPUs with 256 GB RAM/node) on the Dutch national supercomputer Snellius (SURFsara). Note that the wall-clock time of a simulation is longer which, for example, incorporates the time needed for saving data files.

2.5 | CFD solution validation

The LES simulations are performed with the dynamic kinetic energy SGS model.[101] This SGS model was used in a previous paper by the authors,[97] which presented LES simulations in a generic and empty reduced-scale airplane cabin model. The generic flow field incorporated the fundamental flow components/phenomena inherent to opposing-jet MV under isothermal conditions (e.g., supply jets, jet-jet interaction, merged jet, impingement and recirculation zones, laminar-turbulent transitional zones, turbulence anisotropy, and streamline curvature[97]) and the LES simulation results were extensively validated using mean velocity and turbulence measurement data. The study showed a very good performance of LES with the dynamic kinetic energy SGS model, in close agreement with the measurement data. Also, Wang and Chen[102] obtained accurate results using this model in their generic set-up representing half an airplane cabin with inclusion of an obstruction and mixed convection. Following the principle of subconfiguration validation,[103–105] it can be assumed that the LES predictions with the dynamic kinetic energy SGS model will be accurate in the current (more realistic) airplane cabin model as well. In addition, former studies[18,23] that did compare LES simulations with measurements of opposing-jet MV in realistic airplane cabins (both under occupied and non-occupied conditions) confirm the high accuracy of LES.

3 | CONTAMINANT TRANSPORT AND VENTILATION EFFICIENCY

3.1 | Dispersion modeling

Mass transport of passive contaminants (exhaled air by the passengers) is governed by the Eulerian advection–diffusion equation (in Einstein notation):

$$\frac{\partial c}{\partial t} + u_i \frac{\partial c}{\partial x_i} = D_m \frac{\partial^2 c}{\partial {x_i}^2} + s_c \tag{2}$$

where c is the instantaneous (scalar) contaminant concentration (exhaled air), expressed in units of mass of contaminants per unit volume of air (kg/m^3), u_i (m/s) the velocity components (u, v, or w), s_c (kg/m^{3}s) the production of exhaled contaminants (i.e., G_c per unit volume; Section 2.3), and D_m the molecular mass diffusivity (m^2/s).

In LES, the filtered form of Equation 2 is used (i.e., in terms of filtered/resolved variables), which — after application of (time-)averaging — becomes:

$$\frac{\partial}{\partial x_i}\left(Q_{m,i} + Q_{c,i} + Q_{t,i}\right) = S_c \tag{3}$$

Note that S_c is equal to s_c due to the constant rate of contaminant production. $Q_{m,i}$, $Q_{c,i}$, and $Q_{t,i}$ (kg/m^{2}s) represent the components of the mean molecular, convective, and turbulent mass fluxes, respectively, defined as:

$$Q_{m,i} = -D_m \frac{\partial \bar{\tilde{c}}}{\partial x_i} \tag{4}$$

$$Q_{c,i} = \bar{\tilde{u}}_i \bar{\tilde{c}} \tag{5}$$

$$Q_{t,i} = \overline{\tilde{u}_i{}' \tilde{c}'} + \bar{q}_{SGS,i} \tag{6}$$

The overbar indicates time-averaging and the tilde symbol refers to filtered/resolved variables. $Q_{m,i}$ (Equation 4) is the mean contribution of molecular diffusion to the mass transport, related to the gradient of the mean resolved concentration $\bar{\tilde{c}}$. Typically, $Q_{m,i}$ is much smaller than the other mass fluxes (in this study, two to three orders of magnitude) and will therefore not be discussed further. $Q_{c,i}$ (Equation 5) accounts for the advection of $\bar{\tilde{c}}$ by the mean resolved flow ($\bar{\tilde{u}}_i$). $Q_{t,i}$ (Equation 6) encompasses the mean contribution of the resolved (first term) and SGS (second term) fluctuations, with $q_{SGS,i}$ modeled as $-D_{SGS}\frac{\partial \tilde{c}}{\partial x_i}$ in which the SGS mass diffusivity D_{SGS} (m^2/s) is determined as the ratio of the SGS kinematic viscosity ν_{SGS} (m^2/s) and the SGS Schmidt number Sc_{SGS} (−), the latter being dynamically calculated.

Important to mention is that $Q_{t,i}$ in case SV takes into account only the *turbulent* (i.e., random) fluctuations whereas in the cases with TPV, besides the turbulent fluctuations also the large-scale/low-frequency (time-periodic) fluctuations induced by the time-periodic forcing are incorporated. Strictly, referring to $Q_{t,i}$ as a turbulent mass flux in the TPV cases is thus not correct, yet this terminology is remained in the rest of the paper for all simulation cases to allow easier notation. In order to obtain the true turbulent mass fluxes under TPV, triple decomposition has to be performed in which the velocity and concentration variables are decomposed into their mean value, the time-periodic fluctuation and the turbulent fluctuation, which is not considered in this work.

In order to facilitate notation, mean (resolved) variables will be denoted by upper-case letters (e.g., $\bar{\tilde{c}}$ becomes C). The concentrations will be presented in dimensionless form C/C_{ref} with C_{ref} a reference concentration determined as the ratio of G_c to the total (volume) supply flow rate of fresh air. Similarly, for the mass fluxes, a reference flux $Q_{ref} = C_{ref} \cdot U_{0,SV}$ will be used.

3.2 | Ventilation efficiency

The ventilation efficiency[106] often encompasses two indices that represent the performance of a ventilation system regarding the efficiency with which fresh air is supplied to the indoor environment (i.e., the ACE ε_a) and effectiveness of the extraction of contaminants (i.e., the CRE ε_c).

The ACE relates the actual air change time (i.e., the room mean age of air $<\overline{\tau}>$) to the shortest possible air change time (i.e., the nominal time constant τ_n) according to:

$$\varepsilon_a = \tau_n / 2\langle\overline{\tau}\rangle \quad (7)$$

τ_n is determined by the cabin air volume and the total supply flow rate, and $<\overline{\tau}>$ is obtained from the volume-averaged (full cabin volume) local mean age of air $\overline{\tau}$, which is the mean time of supply air to reach a specific location. Note that angle brackets <.> are used to indicate volume-averaging. Following Etheridge and Sandberg,[107] the local mean age of air can be calculated in the case a uniformly distributed (homogeneous) source is present. Therefore, a second source of passive gas is incorporated that is uniformly distributed throughout the entire cabin with a source rate $S_c^* = 10^{-6}$ kg/m^{3}s producing a "background" concentration c^*; note that the star symbol is used to refer to the source rate and concentration related to this uniform source, not to be confused with those of the air exhaled by the passengers mentioned earlier (S_c and c). The local mean age of air is then $\overline{\tau} = C^*/S_c^*$. Inclusion of this source thus solely serves the purpose of calculating the ACE and will be used in Section 4.1 for visual inspection of the distribution of fresh air in the cabin. It does not affect the flow nor the contaminant concentration from the exhaled air. A perfectly mixed flow is characterized by an ACE = 0.5. Further insights into ε_a can be obtained from the local air change index[54] $\varepsilon_{a,p}$:

$$\varepsilon_{a,p} = \tau_n / \overline{\tau} \quad (8)$$

which represents the distribution of $\overline{\tau}$. In the case $\varepsilon_{a,p} > 1$, air is delivered more efficiently to the particular point in the cabin than in a perfect mixing system.

The CRE is an indication of the effectiveness of dilution and removal of contaminants, defined according to:

$$\varepsilon_c = (C_o - C_s) / (< C > - C_s) \quad (9)$$

where the subscripts refer to the outlet (o) and the supply (s). Since no contaminants are present in the supply air, C_s is zero (no recycling of extracted air). In a fully mixed flow, $<C> = C_o$ and $\varepsilon_c = 1$. Short-cut flows, for example, tend to decrease the CRE, whereas induction of piston flow can cause CRE > 1.

4 | COMPUTATIONAL RESULTS

4.1 | Instantaneous flow fields

Figures 4, 5, and 6 provide contours of the dimensionless (instantaneous) velocity magnitude ($|v|/U_{0,SV}$) and corresponding dimensionless background concentration (c^*/S_c^*) in the vertical midplane ($z/H \approx 0.55$) at several instances (indicated as *a*-*d*) over the course of one supply cycle of the inlet velocities for the three ventilation cases, respectively. Corresponding Videos S1–S6 are added to the supporting information section. Again, note that c^* is generated from the uniform source S_c^* (i.e., not from S_c of the exhaled air), the distribution of which provides insights into the delivery of the fresh supply air throughout the cabin. The contaminant concentration induced in the cabin by the exhaled air of the passengers (c) is thus not visible in Figures 4–6, and the concentration levels c^* are solely determined by the uniform source and the fresh supply air. Passengers and seats that are behind the midplane are visualized by the thin white outline and the white plus symbols indicate the location of the passengers' mouths.

The snapshots of case SV (Figure 4; Videos S1, S2) show four times a similar flow pattern, with the opposing jets interacting (collision) and merging into a downward flow (merged jet) at the vertical symmetry plane ($x/H = 0$; Figure 1B). The transient jet interaction causes the merged jet to alternate left and right nearby $x/H = 0$ within the aisle zone. Fresh air then reaches the passenger zone and the zone below the seats (like indicated on the image of instance *a*: $t/T \approx 0.13$).

The characteristic flow patterns in TPV_AS are illustrated in Figure 5 (Videos S3, S4). At instance *a* ($t/T \approx 0.14$), the inlet velocity at the left inlets is close to maximum and at the right inlets it is almost zero. While the left supply jets are developing, vortices are generated below each of the jets and the jets experience the adverse pressure gradient from the counterflow (that is still present from the attenuated right supply jets during the previous supply cycle). At instance *b* ($t/T \approx 0.34$), the left lateral jet is then pushed downwards and high-momentum fresh air directly enters the passenger zone from above the aisle seat. Part of the fresh air also reaches the zone below the seats. As illustrated with instance *c* ($t/T \approx 0.58$), the right inlet velocities have increased in the meanwhile and the developing right supply jets now experience a counterflow (from the attenuated left supply jets), which deflects the right jets downward. Instance *d* ($t/T \approx 0.92$) shows that both right jets eventually propagate further and interact again with the developing opposing left jets. In TPV_AS, the induced time-periodic flow patterns oscillate from side to side. In addition, the vortices developing below the lateral inlets (which are not present in case SV) contribute to the distribution of fresh air above the passengers' heads.

In TPV_SS, shown in Figure 6 (Videos S5, S6), at instance *a* ($t/T \approx 0.14$) the inlet velocity at the lateral inlets increases while it decreases at the ceiling inlets, with the lateral jets developing and interacting at the vertical symmetry plane ($x/H = 0$; Figure 1B). As shown with instances *b* ($t/T \approx 0.34$) and *c* ($t/T \approx 0.58$), the same occurs for the ceiling jets during the subsequent half of the periodic cycle. At instance *d* ($t/T \approx 0.92$), the lateral jet velocity has increased again while this of the ceiling jets has decreased. This creates "pulses" of high-momentum fresh air along the merged jet, which remains localized within the aisle zone. Whereas the merged jet driven by the ceiling jets (instances *a*: $t/T \approx 0.14$, and *d*: $t/T \approx 0.92$) has a relatively narrow width and is characterized by a low concentration, the width of the merged jet formed from the lateral jets is broad and already well-mixed (instances *b*: $t/T \approx 0.34$, and *c*: $t/T \approx 0.58$). Also in this TPV case, vortices below the lateral inlets distribute fresh air to the upper parts of the passenger zone. Vortices developed below the ceiling jets can travel along the merged jet (instance *d*: $t/T \approx 0.92$). Fresh air then becomes distributed from the merged jet to the passenger zone and to below the seats (as indicated at instances *c*: $t/T \approx 0.58$, and *d*: $t/T \approx 0.92$).

4.2 | Mean velocity

Figure 7 shows contours and profile plots of the dimensionless mean velocity magnitude ($|V|/U_{0,SV}$) in (half of) the vertical midplane ($z/H \approx 0.55$; Figure 7A,B) and the horizontal plane at row two ($y/H \approx 0.53$; Figure 7C,D) for the three ventilation cases. Mean velocity vectors are also plotted in Figure 7A. In Figure 7E, the volume-averaged dimensionless mean velocity magnitudes ($<|V|>/U_{0,SV}$) obtained in the full cabin (image 1) and subzones (images 2–7) of case SV are reported, together with the corresponding percentage changes for the two TPV cases with respect to case SV. The subzones encompass the passenger zones (images 2–5), the zone below the seats (image 6), and the aisle zone (image 7), of which the dimensions are as indicated (the height of the aisle zone is based on ASHRAE guidelines[64]). Each zone covers the full length of the cabin (*L* in Figure 1A).

All cases show a recirculation cell above the seats, with the flow below the seats directed toward the outlets, part of which is extracted at the outlet and part of which flows back upwards along the sidewalls (return flow). A clear difference between TPV with respect to SV is the overall increased velocity levels (Figure 7A,B); especially above the passenger seats ($0.3 < y/H < 0.4$) and in the aisle seat zone in TPV_AS, and in the aisle zone, below the seats and near the sidewall in TPV_SS, in line with the instantaneous flow behavior (Figures 4–6; Videos S1–S6). Furthermore, an increased width of the lateral supply jets is observed, and the size of the low-velocity center of the recirculation cell, located in between the middle ($x/H \approx -0.45$) and aisle ($x/H \approx -0.23$) seat passengers, is reduced. Figure 7C indicates more clearly that this reduction is much stronger in TPV_AS. In Figure 7C,D, the local high-velocity areas right in front of the passengers' heads show the core of the exhaled air jets (expiratory plumes) from the mouths (which in Figure 7B are visible as peaks at $y/H \approx 0.53$).

A quantitative comparison of the velocity levels in the different cases is presented in Figure 7E. $<|V|>/U_{0,SV}$ over the full volume (image 1) increases with 13% and 30% in TPV_AS and TPV_SS, respectively. Within the passenger zone (images 2–4), the increase in velocity magnitude depends on the case (TPV_AS or TPV_SS) and the seat zone (window, middle or aisle seat): in TPV_AS, $<|V|>/U_{0,SV}$ increases the most in the middle (+55%) and aisle (+52%) seat zones, whereas in TPV_SS, the increase is highest in the window (+43%) and middle (+36%) seat zones. In all cases (SV and TPV), the mean velocity magnitude decreases from the aisle seat toward the window seat zone. The velocity increase in the total passenger zone (image 5) amounts 49% (TPV_AS) and 31% (TPV_SS). Below the seats (image 6) the velocity level strongly increases (+34%) in TPV_SS only. Similarly, in the aisle zone (image 7), $<|V|>/U_{0,SV}$ increases by 39% in TPV_SS, in contrast to TPV_AS for which a reduction of 19% is noted.

4.3 | Mean exhaled contaminant concentration

Figure 8 presents the distributions of the dimensionless mean exhaled contaminant concentration (C/C_{ref}) in cases SV and TPV — again, not to be confused with c^* shown in Figures 4–6 — using contours (with isolines) and profiles in the vertical midplane (Figure 8A,B) and in the horizontal plane (Figure 8C,D). Volume-averaged values ($<C>/C_{ref}$) in case SV and corresponding percentage changes in the two TPV cases are reported in Figure 8E.

Figure 8A–D shows that in all ventilation cases, relatively high concentration levels are observed around the contaminant sources in the vertical midplane (mouths of passengers; $0.4 < y/H < 0.7$ in Figure 8A,B) and in front of the passengers ($0.51 < z/H < 0.73$ in Figure 8C,D). In the supply jet areas (i.e., right below and in between the OHSCs; $y/H > 0.7$) and in the aisle zone, the concentration levels are relatively low.

TPV reduces the concentrations around the sources compared with SV, as for example shown by the reduced peak values in Figure 8B ($y/H \approx 0.53$). Whereas the reduction at the middle seat ($x/H \approx -0.45$) is similar in both TPV cases, the peak concentration at the aisle seat reduces more in TPV_AS ($x/H \approx -0.23$), while at the window seat ($x/H \approx -0.67$), it reduces more in TPV_SS. Also in the horizontal plane, the overall decrease in concentration under TPV compared with SV is noted. Especially within the low-velocity recirculation cell center in case SV in front/between the heads of the middle and aisle seat passengers (cf. Figure 7C), the concentration level strongly reduces (green colored zones in Figure 8C). In the upper parts of the cabin (Figure 8B; $y/H > 0.7$, $x/H > -0.45$) the concentration in TPV_SS increases to above this of case SV, and is higher than in TPV_AS.

Figure 8C,D furthermore shows a strong reduction in the horizontal (longitudinal) penetration depth of the high-concentration expiratory plumes under TPV, clearly visible from the isolines in Figure 8C or the much faster concentration decay along the horizontal sampling lines in Figure 8D. Figure 9 provides a further visualization of the mean expiratory plume shape in the vertical cross-section of each passenger (using isolines of C/C_{ref} in Figure 9A–C) and throughout the cabin (isosurface $C/C_{ref} = 2$ in Figure 9D) for the three ventilation cases. The (3D) mean velocity vectors are also

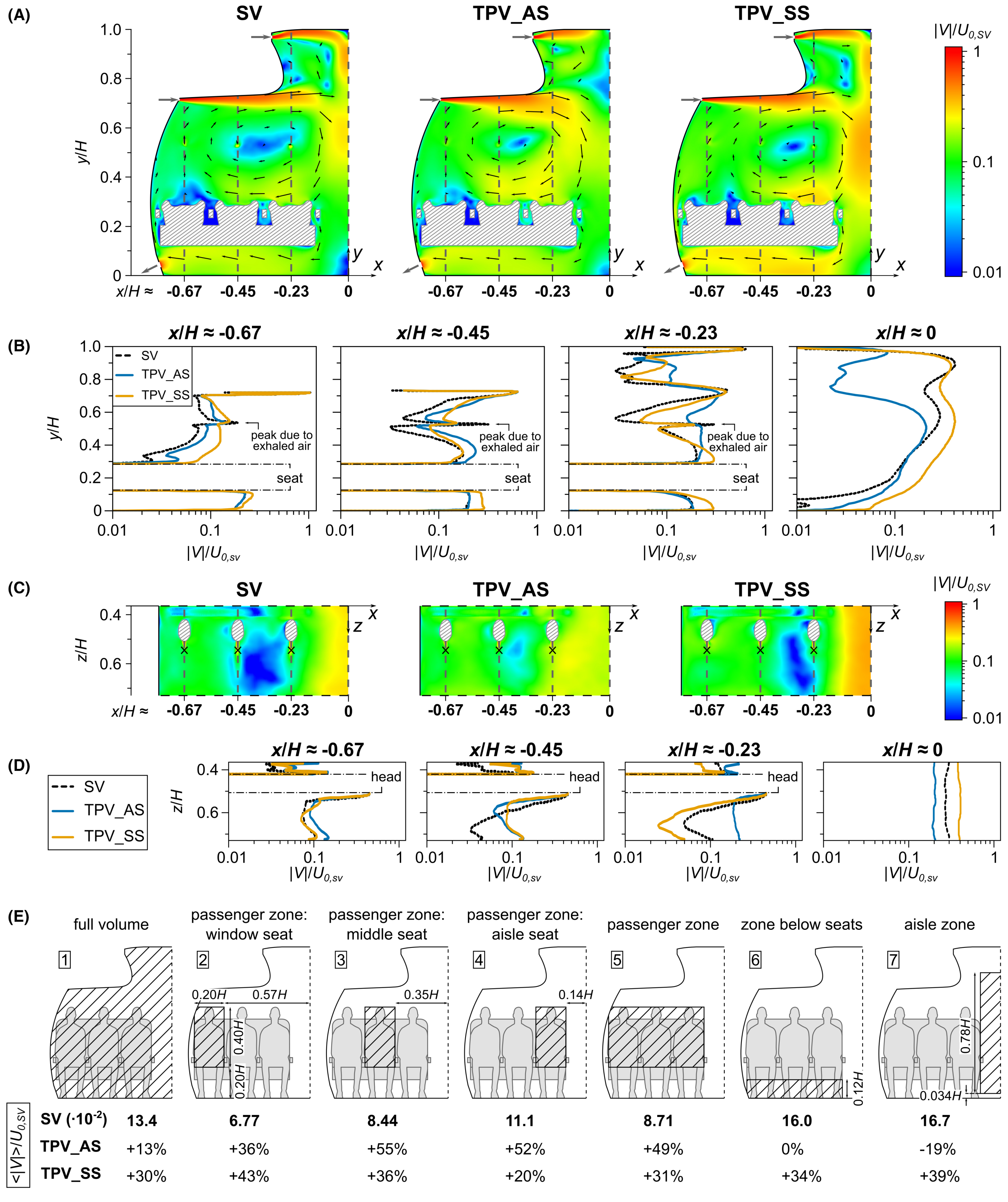

FIGURE 7 Dimensionless mean velocity magnitude ($|V|/U_{0,SV}$) in SV, TPV_AS and TPV_SS: (A) contours and velocity vectors in vertical midplane ($z/H \approx 0.55$); (B) profile plots along vertical sampling lines shown in (A); (C) contours in horizontal plane ($y/H \approx 0.53$); (D) profile plots along horizontal sampling lines shown in (C), with cross symbols indicating location of vertical sampling lines; (E) volume-averaged velocity magnitude ($<|V|>/U_{0,SV}$) in full volume and subzones of SV with corresponding percentage changes in TPV cases

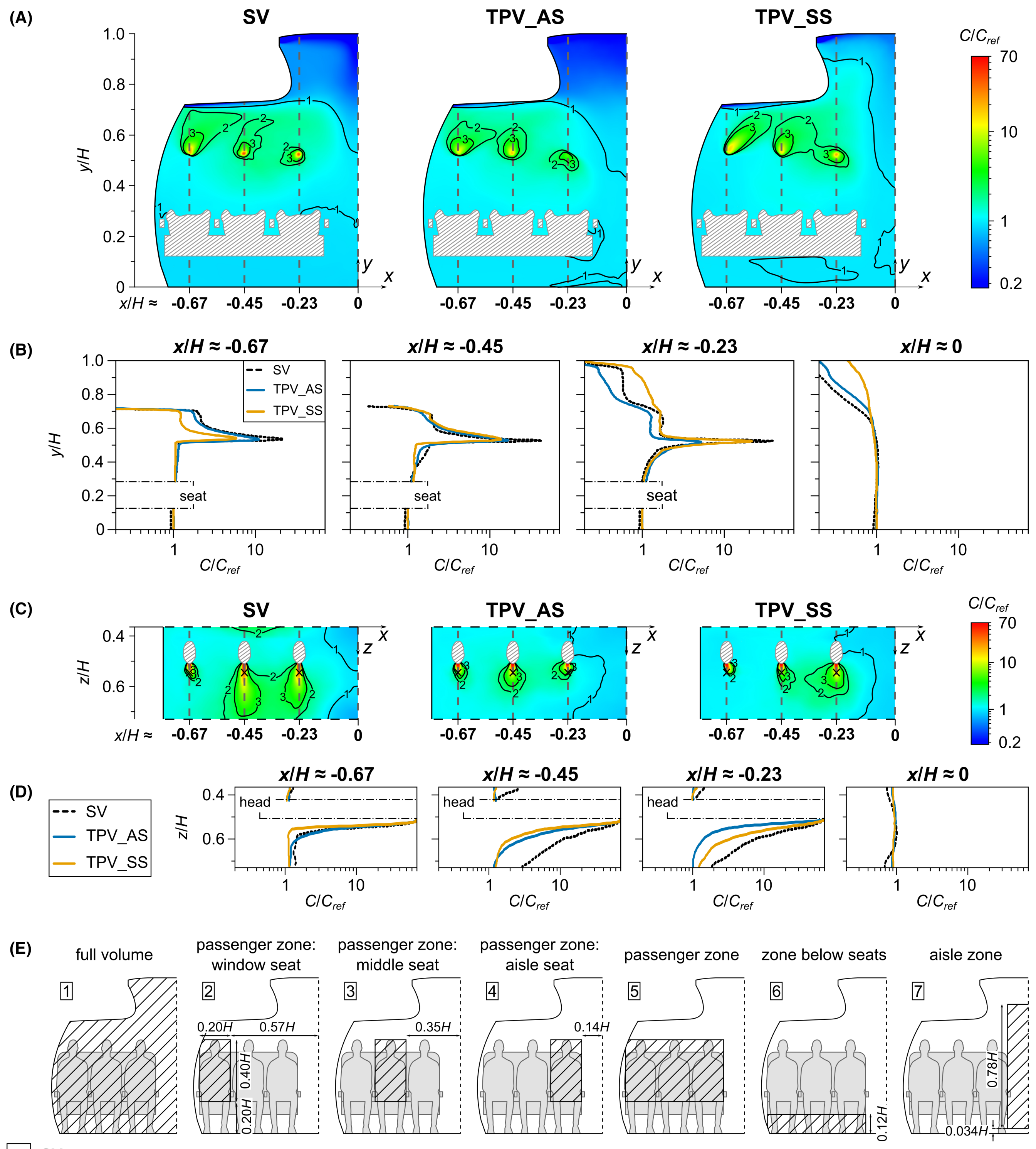

<C>/C_ref	1	2	3	4	5	6	7
SV	1.17	1.32	1.69	1.53	1.51	0.945	0.886
TPV_AS	-12%	-7%	-21%	-23%	-18%	+7%	+2%
TPV_SS	-5%	-11%	-23%	-12%	-16%	+5%	+8%

FIGURE 8 Dimensionless mean exhaled contaminant concentration (C/C_{ref}) in SV, TPV_AS, and TPV_SS: (A) contours in vertical midplane ($z/H \approx 0.55$); (B) profile plots along vertical sampling lines show in (A); (C) contours in horizontal plane ($y/H \approx 0.53$); (D) profile plots along horizontal sampling lines shown in (C), with cross symbols indicating location of vertical sampling lines; (E) volume-averaged concentration ($<C>/C_{ref}$) in full volume and subzones of SV with corresponding percentage changes in TPV cases. Isolines of C/C_{ref} are also shown in (A) and (C).

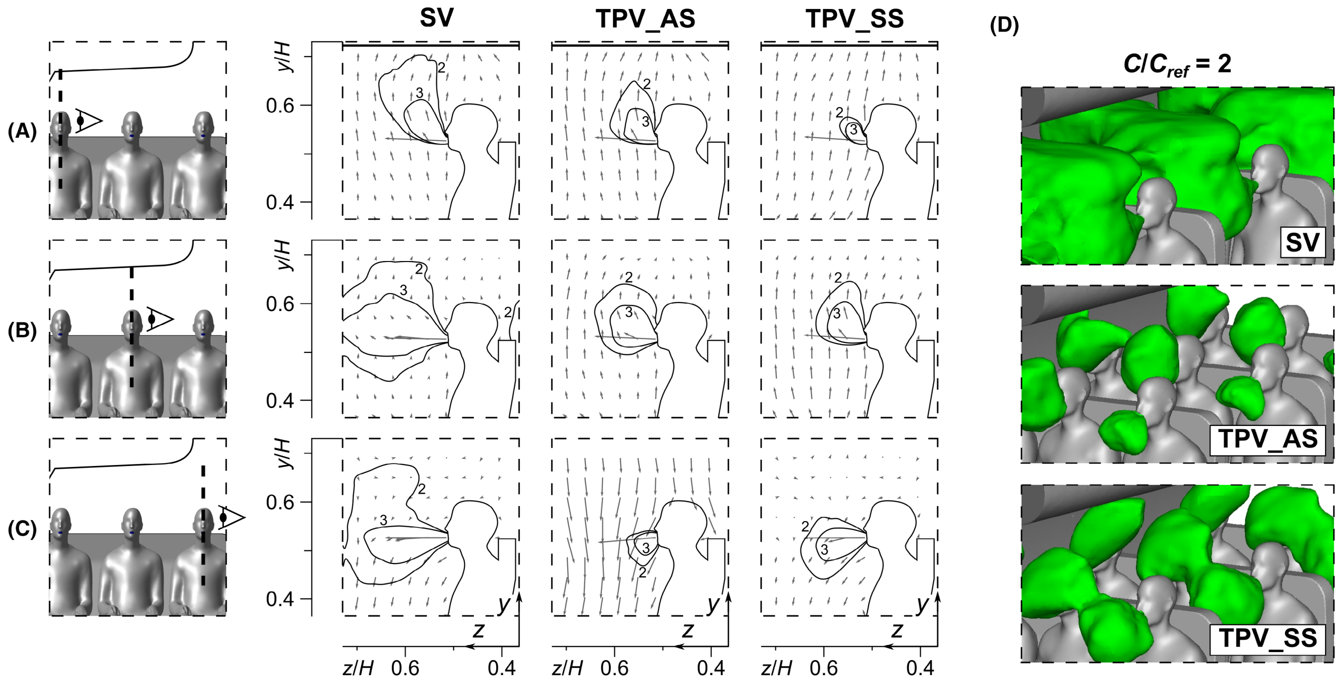

FIGURE 9 Isolines of dimensionless mean exhaled contaminant concentration (C/C_{ref}) and mean velocity vectors in vertical cross-sections of (A) window, (B) middle, and (C) aisle seat passengers, and (D) isosurface $C/C_{ref} = 2$ in SV, TPV_AS, and TPV_SS

shown in Figure 9A–C. In all ventilation cases, the orientation of the plumes is according to the mean recirculation flow (Figure 7A): plumes of the aisle seat passengers are directed downwards while at the middle and window seats the plume direction is upwards. Their reduced spatial extent under TPV indicates a better dilution of the exhaled concentration compared to case SV, caused by the time-periodic flow patterns that perturb the plumes' flow direction. Noteworthy is the strongly diluted plume of the aisle seat passenger in TPV_AS (Figure 9C), surrounded by the strong downflow (cf. Figure 5B). In TPV_SS, the decreased longitudinal penetration of the passengers' plumes at the window and middle seats (Figures 9A,B and 8C) compared with TPV_AS may be attributed to the somewhat stronger upward (return) flow in this case (see vectors and profiles at $x/H = -0.67$ and -0.45 in Figure 7A,B), which in addition results in more prolonged plumes that are deflected away further from the sidewall (see Figure 9D and isolines in Figure 8A).

A quantitative view of the changes in concentration levels using TPV compared with SV is obtained from $<C>/C_{ref}$ in Figure 8E. In the full volume (image 1), $<C>/C_{ref}$ decreases more in TPV_AS (−12%) than in TPV_SS (−5%), with a decrease of 18% and 16% in the passenger zone (image 5), respectively. Within the passenger zone, the reduction in the concentration level varies per seat zone (images 2–4): in TPV_AS, the reduction is highest at the aisle (−23%) and middle seat (−21%) zones, whereas in TPV_SS the middle seat zone is affected most (−23%). In terms of absolute concentration levels, in SV and TPV_AS $<C>/C_{ref}$ is highest at the middle seat. The lowest concentrations in these two cases are observed for the window seat and aisle seat, respectively. In TPV_SS, $<C>/C_{ref}$ decreases from the aisle seat toward the window seat. On the contrary, below the seats (image 6) and in the aisle zone (image 7), TPV results in increased

TABLE 1 Concentration in the outlet air (C_o/C_{ref}) and performance indicators (ε_c and ε_a) in case SV, together with corresponding percentage change in TPV cases

	SV	TPV_AS	TPV_SS
C_o/C_{ref} [−]	0.96	+6%	+4%
ε_c [−]			
• Full volume	0.83	+20%	+9%
• Passenger zone	0.64	+28%	+23%
ε_a [−]	0.54	+7%	−4%

concentrations (+2% to 8%), indicating transport of contaminants from the passenger zone toward the surrounding zones.

As outlined in Table 1, the concentration at the outlets in the TPV cases increases compared to case SV, which, together with the decreased contaminant concentrations within the cabin (subzones), results in an increased ε_c (Equation 9). In the full cabin volume, the increase amounts 20% (TPV_AS) and 9% (TPV_SS), and in the passenger zone 28% (TPV_AS) and 23% (TPV_SS). In addition, Table 1 shows ε_a (Equation 7), which equals 0.54 in case SV. An increased ε_a is observed for TPV_AS (+7%), whereas in TPV_SS ε_a decreases (−4%). The latter is caused by a strong decrease (−28%; not shown in Table 1) of the local air change index $\varepsilon_{a,p}$ (Equation 8) in the upper part of the cabin in between the OHSCs ($y/H > 0.7$) and in the aisle zone (−11%) in this case compared with case SV, due to the (ceiling) supply jets that do not continuously provide fresh air to these zones of the cabin unlike in cases SV and TPV_AS (see e.g., instance b: $t/T \approx 0.34$ in Figure 6). However, in the passenger zones $\varepsilon_{a,p}$ does increase (although weakly, +2%) with respect to SV, indicating that the delivery of fresh air to the passengers occurs more efficiently.

This of course also holds for TPV_AS, which shows an up to 14% increase of $\varepsilon_{a,p}$ in the passenger zone.

4.4 | Mean exhaled contaminant mass fluxes

Figures 10 and 11 show contours of the dimensionless mean convective (Equation 5) and turbulent (Equation 6) mass flux components, respectively, for the three ventilation cases. Isolines of C/C_{ref} are also shown. Note that the turbulent mass flux components in the TPV cases incorporate both the time-periodic as well as the random (turbulent) fluctuations, as mentioned earlier. In all ventilation cases, convection appears to be the dominant mass transport mechanism, which, in the vertical midplane (Figure 10A,B), is the highest (in terms of absolute values) within the supply jets and the flow above/below the passenger seats ($Q_{c,x}/Q_{ref}$, Figure 10A), and in the aisle zone and near the sidewall ($Q_{c,y}/Q_{ref}$, Figure 10B). In the horizontal plane (Figure 10C), high (positive) fluxes in the longitudinal direction ($Q_{c,z}/Q_{ref}$) emanate from the sources (expiratory plumes).

Figure 10A indicates an increased (negative) $Q_{c,x}/Q_{ref}$ (i.e. flux toward the left) in TPV_AS in between/below the source locations of the middle and aisle seat passengers (number I in Figure 10A; $-0.45<x/H<-0.23$, $y/H\approx0.5$) compared with case SV, induced by the downflow described earlier (see instance *b*: $t/T\approx0.34$ of Figure 5). In TPV_SS, higher (positive) $Q_{c,x}/Q_{ref}$ are observed at the source location of the window seats (small very dark red area with

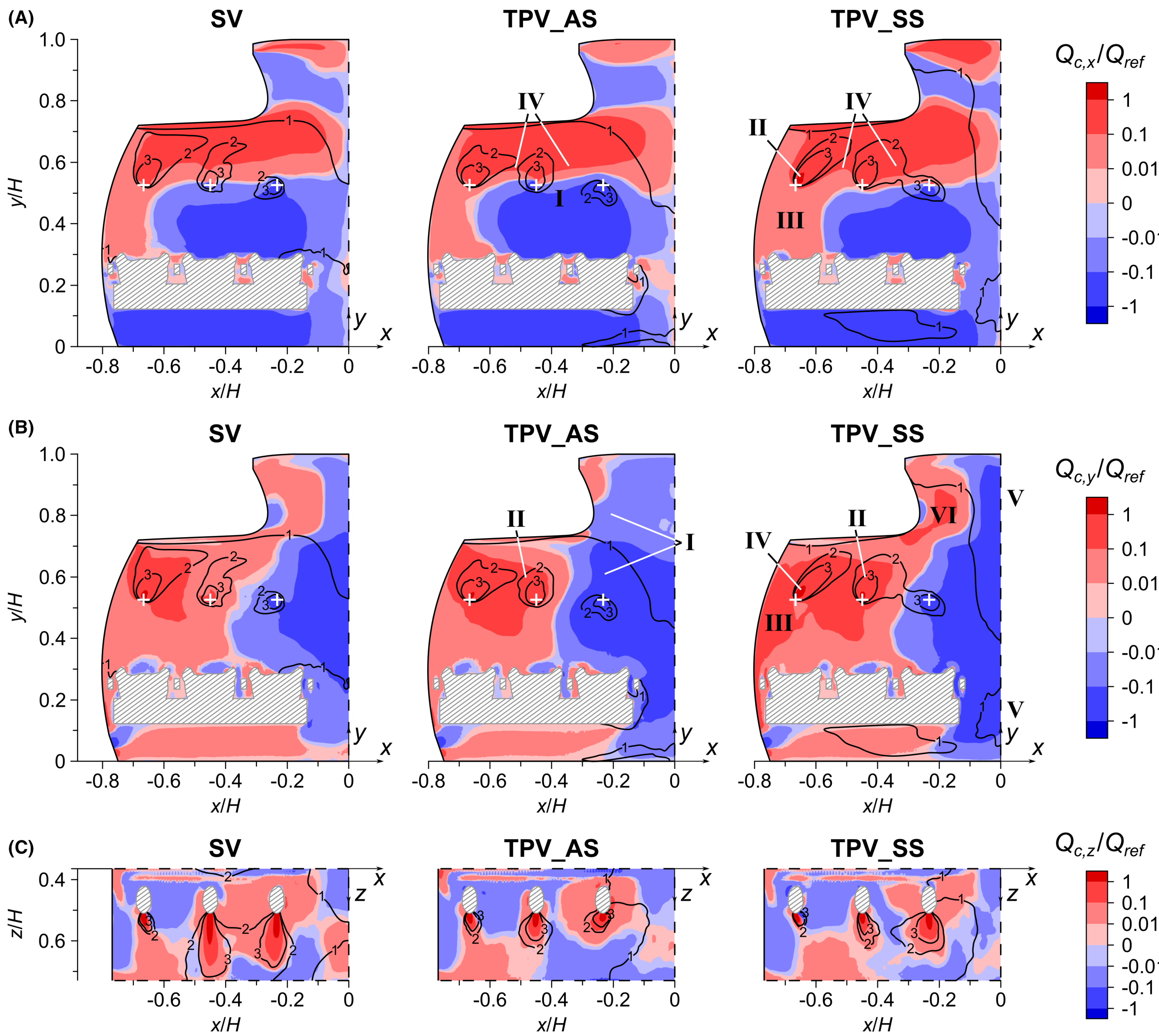

FIGURE 10 Contours of dimensionless mean convective mass fluxes in (A) *x*-direction ($Q_{c,x}/Q_{ref}$) and (B) *y*-direction ($Q_{c,y}/Q_{ref}$) in vertical midplane ($z/H\approx0.55$), and in (C) *z*-direction ($Q_{c,z}/Q_{ref}$) in horizontal plane ($y/H\approx0.53$) for SV (left), TPV_AS (middle), and TPV_SS (right). Isolines of C/C_{ref} are shown as well. The white plus symbols in (A,B) indicate source locations (mouth) at $x/H\approx-0.23$, -0.45 and -0.67. Numbers I–VI indicate specific regions mentioned in text.

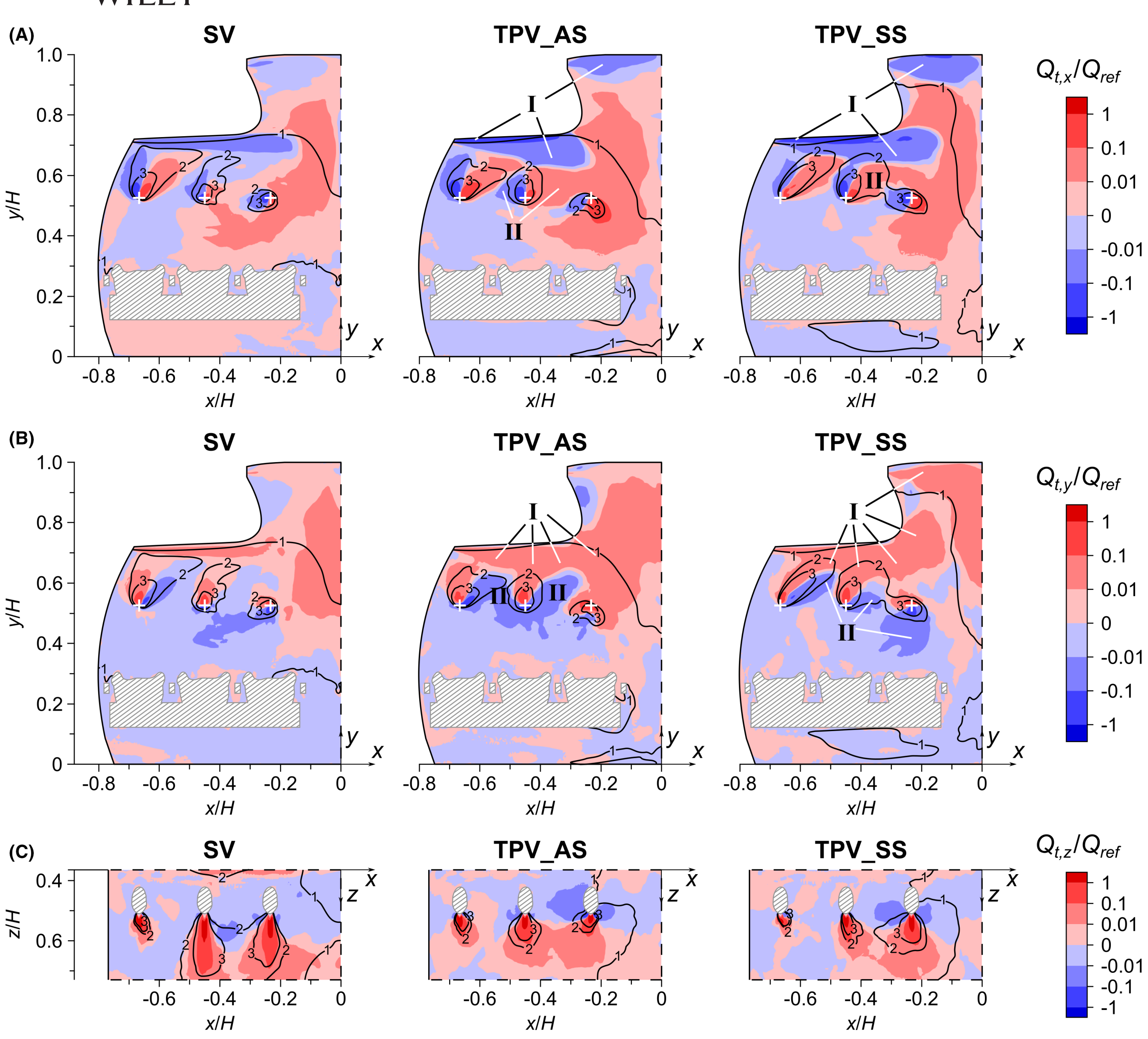

FIGURE 11 Contours of dimensionless mean turbulent mass fluxes in (A) *x*-direction ($Q_{t,x}/Q_{ref}$) and (B) *y*-direction ($Q_{t,y}/Q_{ref}$) in vertical midplane ($z/H \approx 0.55$), and in (C) *z*-direction ($Q_{t,z}/Q_{ref}$) in horizontal plane ($y/H \approx 0.53$) for SV (left), TPV_AS (middle), and TPV_SS (right). Isolines of C/C_{ref} are shown as well. The white plus symbols in (A,B) indicate source locations (mouth) at $x/H \approx -0.23$, -0.45 and -0.67. Numbers I and II indicate specific regions mentioned in text.

$Q_{c,x}/Q_{ref} > 1$ at plus symbol, indicated with number II in Figure 10A), and the area below containing positive flux increases in width (number III in Figure 10A; $x/H < -0.60$, $0.28 < y/H < 0.53$), which could be attributed to the stronger return flow noticed for this case. In both TPV cases, slightly increased (positive) fluxes are also observed above the source locations ($0.53 < y/H < 0.60$; numbers IV) in the area affected by the lateral supply jets.

Figure 10B shows that differences in $Q_{c,y}/Q_{ref}$ between the TPV cases and case SV are more distinct. TPV_AS is characterized by a much stronger downward (negative) flux above the aisle seat (number I in Figure 10B) and an increased positive flux above the middle source location ($x/H \approx -0.45$; number II); cf. instances *b-d*: $t/T \approx 0.34$–0.92 in Figure 5. The latter is also true for TPV_SS (number II in Figure 10B; see also instance *c*: $t/T \approx 0.58$ in Figure 6), which in addition shows increased (positive) fluxes near the sidewall (number III), in particular at the source location of the window seat passenger (small very dark red area with $Q_{c,y}/Q_{ref} > 1$ at plus symbol, indicated with number IV). An increased downward flux in the upper ($y/H > 0.7$) and lower ($y/H < 0.2$) areas of the aisle zone (numbers V), and an increased upward flux along the OHSC (number VI) are also observed for this case.

Figure 10C shows a clear reduction of the longitudinal mean convective fluxes ($Q_{c,z}/Q_{ref}$) of the expiratory plumes with TPV compared with SV. Whereas in TPV_AS the extent of the aisle and middle seat passengers' plumes strongly reduces, in TPV_SS mainly those of the middle (and to a lesser extent of the window and aisle) seat passengers are affected, which is in line with the results presented in Figure 8C,D and Figure 9. The relative magnitude of $Q_{c,z}$ with respect to $Q_{c,x}$ and $Q_{c,y}$ (Figure A1 in Appendix A) indicates that $Q_{c,z}$ is at least an order of magnitude smaller than $Q_{c,x}$ and $Q_{c,y}$ in the supply jet area ($y/H > 0.7$), in the aisle zone, below the seats and in parts of the passenger zone (all ventilation cases). Areas where $|Q_{c,z}/Q_{c,x}|$ and $|Q_{c,z}/Q_{c,y}|$ are both larger than unity are rather limited and mainly present around the passengers' heads (expiratory plumes), the spatial extent of which reduces using TPV (Appendix A).

Figure 11 presents distributions of the turbulent mass flux components in the vertical midplane ($Q_{t,x}/Q_{ref}$ and $Q_{t,y}/Q_{ref}$) and in the horizontal plane ($Q_{t,z}/Q_{ref}$) for the three ventilation cases. Although both the resolved and modeled (SGS) contributions (Equation 6) are taken into account, it is interesting to note that the latter is verified to be at least three orders of magnitude smaller than the former due to the high grid resolution applied. In all ventilation cases, $Q_{t,x}/Q_{ref}$ and $Q_{t,y}/Q_{ref}$ (Figure 11A,B) are — in terms of absolute values — the highest within the supply jets, the aisle zone ($y/H > 0.4$) and around the source locations. High (positive) values of $Q_{t,z}/Q_{ref}$ (Figure 11c) are present in the expiratory plumes.

Figure 11A,B shows similar trends in $Q_{t,x}/Q_{ref}$ and $Q_{t,y}/Q_{ref}$ for both TPV cases compared to case SV. TPV leads (in terms of absolute values) to increased turbulent fluxes in most of the supply jets compared with SV (indicated with numbers I in Figure 11A,B), attributed to higher turbulence levels resulting from the stronger shearing forces (due to the rapidly changing inlet velocity (gradients)) and the time-periodic flow patterns. Furthermore, the relatively high (positive/negative) turbulent fluxes at most of the source locations in case SV cover an extended area with TPV (dark red/blue areas where $|Q_{t,x}/Q_{ref}|$ and $|Q_{t,y}/Q_{ref}|$ are in between 0.1 and 1 surrounding the white plus symbols), which demonstrates the increased perturbations of the expiratory plumes by the time-periodic flow patterns. The turbulent fluxes at the source locations point away from the source, indicating that turbulent mass transport operates as a diffusion mechanism from high to low concentrations. The areas surrounding the source locations also obtain increased fluxes (numbers II in Figure 11A,B), in particular around these of the middle ($x/H \approx -0.45$) and aisle ($x/H \approx -0.23$) seat passengers.

According to Figure 11C, TPV reduces the turbulent transport in the longitudinal direction ($Q_{t,z}/Q_{ref}$) in front of the passengers (dark red color in expiratory plumes where $Q_{t,z}/Q_{ref} > 0.1$) compared to SV. Again, in TPV_AS, the reduction in the middle and aisle passenger zones is the largest, whereas in TPV_SS $Q_{t,z}/Q_{ref}$ mainly reduces in the middle passenger zone (although also the window and aisle zones show decreased positive values). At both sides of each source, the negative flux areas ($-0.1 < Q_{t,z}/Q_{ref} < -0.01$) appear to grow, especially for the aisle seat passenger.

Figure 12 presents the relative magnitude of the total turbulent and convective fluxes (Q_t/Q_c) in the vertical midplane (Figure 12A) and the horizontal plane (Figure 12B) for each ventilation case. In all cases, in most of the cabin (49%–61% of the data points in the two planes) Q_t is at least an order of magnitude smaller than Q_c ($Q_t/Q_c < 0.1$, mainly in lower half of the cabin). Figure 12A shows that with TPV, Q_t increases with respect to Q_c within the supply jet area ($y/H > 0.7$; light gray color with $Q_t/Q_c > 0.1$). However, the areas at which $Q_t > Q_c$ (white colored in Figure 12A,B) remain limited (<3% of the data points in the two planes, mainly located close to the source locations and in confined areas in between the OHSCs); note

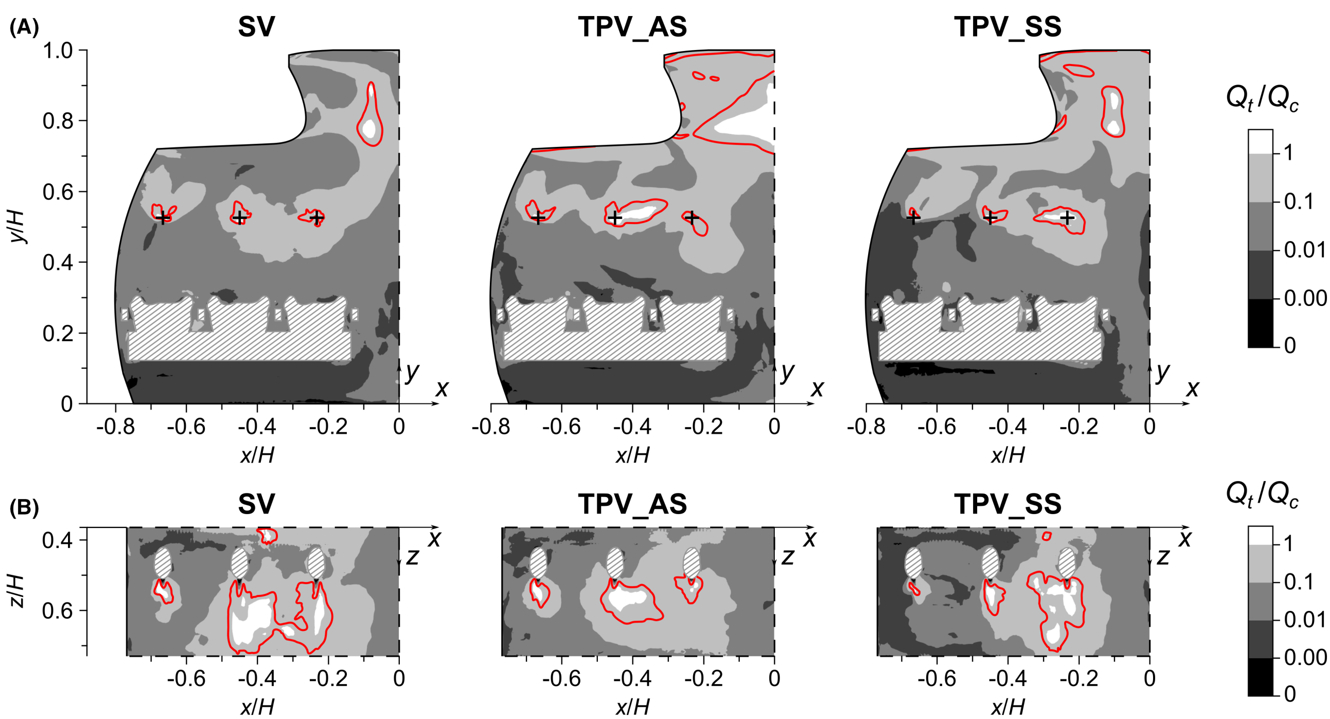

FIGURE 12 Contours of ratio of total turbulent to convective mass flux (Q_t/Q_c) in (A) vertical midplane ($z/H \approx 0.55$) and (B) horizontal plane ($y/H \approx 0.53$) for SV (left), TPV_AS (middle), and TPV_SS (right). The black plus symbols in (A) indicate source locations (mouth) at $x/H \approx -0.23$, -0.45 and -0.67. The isoline $Q_t/Q_c = 0.5$ (red color) is also shown.

that the isoline $Q_t/Q_c = 0.5$ (red color) is also shown as a reference. On the contrary, as indicated by the isoline and the size of the white colored areas in Figure 12B, Q_t reduces in magnitude with respect to Q_c within the expiratory plumes of the aisle and middle seat passengers in TPV_AS, and of the window and middle seat passengers in TPV_SS. In the latter case, Figure 12A,B shows that most of the area nearby the window ($x/H < -0.7$ and $0.3 < y/H < 0.5$) obtained a reduced relative magnitude (dark gray color with $Q_t/Q_c < 0.01$).

5 | DISCUSSION AND FUTURE WORK

Both TPV strategies induce time-periodic airflow patterns, which promote the delivery of fresh air to the passenger zone, thereby also perturbing the passengers' expiratory plumes. As a result, both convective and turbulent contaminant transport (the latter to be interpreted according to the aforementioned clarification) within the vertical plane enhance, while the longitudinal convective and turbulent transport within the expiratory plumes becomes more restricted, causing a rapid dilution of the exhaled contaminant concentration and a distribution of contaminants from the passenger zone to surrounding areas. In addition, the poorly ventilated center of the recirculation cell reduces. This leads to an overall reduction in the mean concentration levels, an augmented extraction of contaminants from the cabin and a more effective mixing of fresh air with cabin air, reflected by the higher ACE (or at least an increased local air change index in the passenger zone) and CRE. Hence, an improved ventilation efficiency can be realized without increasing the total supply flow rate compared with conventional SV.

The potential of TPV for improved cabin air quality may advocate a reduction of the total time-periodic supply flow rate, in order to decrease the costly extraction of bleed air to improve energy savings; in conventional airplane ventilation, the total supply flow rate prescribed by the ASHRAE standard[2] is actually set even slightly higher to compensate for expected locally lower ACE. Furthermore, implementation of time-periodic ventilation does not require a full redesign of the ventilation system, as may be the case for alternative ventilation methods (DV or PV), which is beneficial for existing airplanes. Of course, not only MV, but also alternative ventilation methods may reveal improved performance under time-periodic inlet conditions. Furthermore, the air quality in other enclosures, such as cars, trains, and buildings, may be improved by operation of time-periodic supplies.

However, some limitations to this study have been identified which require future work to further explore the potential of time-periodic inlet conditions:

- Future work should evaluate different periods and amplitudes of the supply flow rate. These parameters can have a strong impact on the ventilation efficiency,[78,79] as well as on the passengers' thermal sensation and comfort[108–111] or on acoustic noise.[61] With the current inlet parameters, air at high-momentum penetrates into the passenger zone (e.g., downflow above the aisle seat passenger in TPV_AS) or aisle zone (pulsated merged jet in TPV_SS), which may increase the draft risk for seated or standing passengers. Lowering the amplitude (which is at maximum value in this study) and/or adjusting the period may help in this respect. As outlined in Table 2, the velocity levels recorded at the (seated) passengers' ankles and chests do not exceed the ASHRAE threshold value of 0.36 m/s,[2,64] although at ankle level (which is a draft-sensitive body area) the velocity is preferred to be lower than 0.20 m/s, which is not the case in TPV_SS. In addition, thermal discomfort may also be caused by the higher cooling effect on the human body when subjected to fluctuating air velocities.[108–111] However, this may equally well provide an opportunity to increase the design temperature of the TPV system (which under SV is usually set low enough to provide sufficient cooling) to counteract the stronger cold sensation, thereby also reducing the energy demand as less cooling of the supply air is needed.
- Although for opposing-jet configurations several studies pointed out that thermal effects are of secondary importance[19,21,29,57] due to the dominant influence of the supply jets (Section 1), non-isothermal conditions should also be examined in which thermal plumes of passengers and conditioning of the airsupply air temperature are considered. Incorporation of heat loads can be important as it is the main factor that determines the required supply flow rate.[1,51] Thermal comfort indicators, the HRE and the dynamic performance[50,59] could then be derived. Also, thermal plumes raising above the passengers will interfere with the ventilation flow, the impact of which depends on their relative strength.[112–114] The — under SV dominant — supply jets may lose some strength when the TPV supply flow rate temporarily decreases. However, the overall impact may be moderate in the case of high amplitudes and/or short periods of the supply flow rate (as in this study), although future work is needed in this respect.
- Although convection is the dominant contaminant mass transport mechanism, future simulations could incorporate triple decomposition to distinguish between the turbulent transport related to the random fluctuations and the transport driven by the low-frequency time-periodic fluctuations.
- Large eddy simulation is used for its accurate prediction of the transient opposing-jet interaction and turbulence characteristics,[97] which is expected to provide improved predictions of the convective and turbulent mass fluxes compared to steady RANS. For case SV, a comparison of C/C_{ref} between LES and RANS is provided in Figure 13. Although the overall concentration distribution obtained with RANS shows similarities with this of the LES prediction (root-mean-square deviation measured over the two planes is 2.87), local differences can be high, for example, at the source locations. This may be explained by, for example, the incapability of steady RANS to capture the influence of unsteady flow phenomena (e.g., transient opposing-jet interaction, fluctuations of expiratory plumes), and/or the inaccurate turbulence modeling, thereby affecting the convective and turbulent mass transport. False predictions related to the improper use of the standard gradient-diffusion hypothesis[115,116] are assessed to be negligible

TABLE 2 Mean velocity magnitude (|*V*|) with standard deviation σ and maximum value (m/s) in the vertical midplane ($z/H \approx 0.55$) at monitoring points located near the window ($x/H \approx -0.67$), middle ($x/H \approx -0.45$), and aisle ($x/H \approx -0.23$) seat passengers, at ankle level ($y/H \approx 0.045$) and at chest height ($y/H \approx 0.40$)

		Window seat		Middle seat		Aisle seat	
		$\|V\| \pm\sigma$	Maximum	$\|V\| \pm\sigma$	Maximum	$\|V\| \pm\sigma$	Maximum
Chest	*SV*	0.07 ±0.023	0.11	0.12 ±0.041	0.17	0.16 ±0.047	0.26
	TPV_AS	0.10 ±0.034	0.15	0.18 ±0.049	0.27	0.21 ±0.069	0.34
	TPV_SS	0.11 ±0.026	0.14	0.14 ±0.045	0.21	0.18 ±0.066	0.31
Ankle	*SV*	0.16 ±0.026	0.20	0.17 ±0.031	0.21	0.16 ±0.031	0.20
	TPV_AS	0.15 ±0.035	0.20	0.16 ±0.030	0.21	0.15 ±0.032	0.20
	TPV_SS	0.19 ±0.052	0.27	0.22 ±0.047	0.30	0.23 ±0.036	0.30

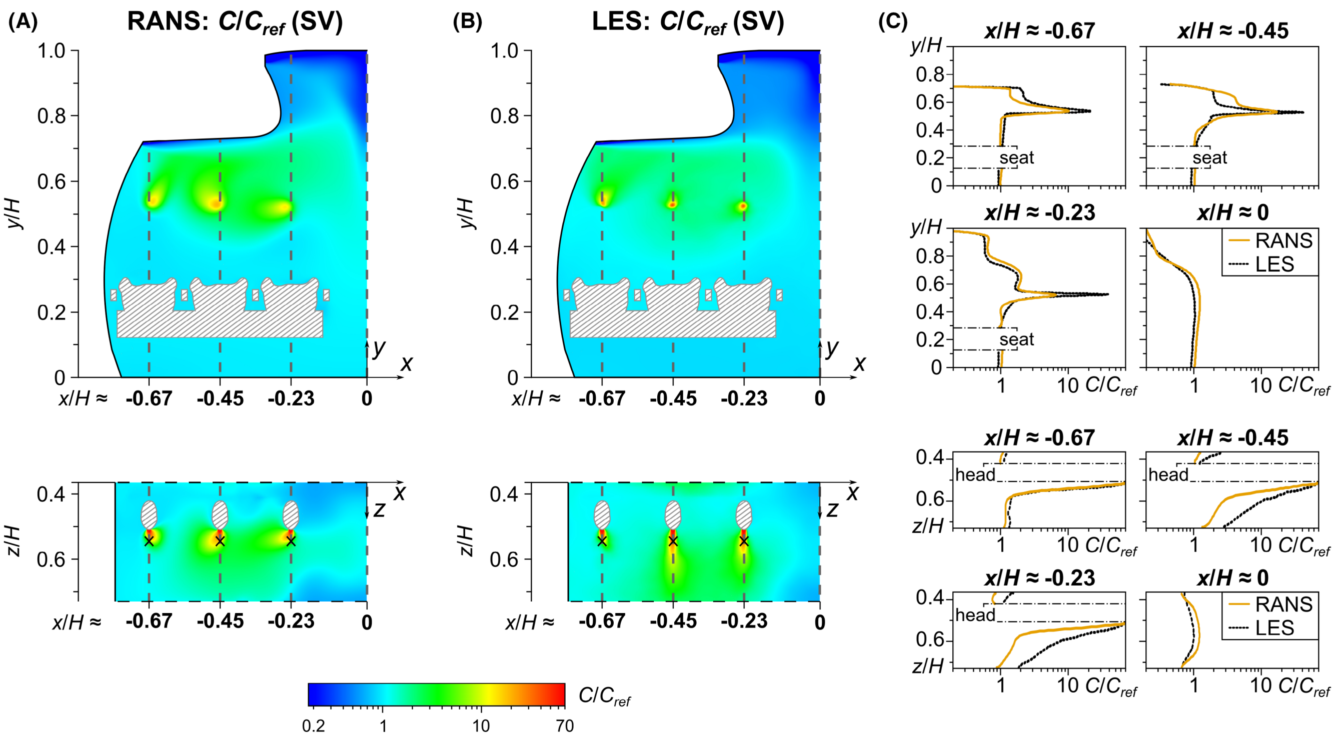

FIGURE 13 Contours (A,B) and profiles (C) of dimensionless mean exhaled contaminant concentration (C/C_{ref}) obtained in RANS simulation (A,C) and LES simulation (B,C) of case SV in vertical midplane at $z/H \approx 0.55$ (top) and horizontal plane at $y/H \approx 0.53$ (bottom)

in this study (Appendix B). Evidently, future work should consist of the validation of contaminant concentrations and mass fluxes. Focusing on different RANS models and unsteady RANS simulations, and/or time-efficient calculation algorithms such as fast fluid dynamics (FFD),[117] will also be valuable given the long simulation time of LES.

- Although TPV improves the dispersion of (gaseous) contaminants, it may likewise increase the risk of cross contamination[23,75] (due to the dynamic flow patterns it induces). Future work should focus on the spread of droplets/aerosols introduced by one or multiple index patients through breathing, coughing, or sneezing, with an assessment of the risk of infection to the surrounding passengers (see e.g., refs. in Section 1). Also, more realistic breathing patterns, real gaseous contaminants (CO_2, CO, and ozone) or humidity conditions could be considered.
- Actual implementation of time-periodic MV in a realistic cabin (mock-up) allows to validate its capabilities under realistic boundary conditions. Information on the diffuser power, cooling/heating capacity and potential energy savings can be gathered,[118] as well as (subjective) comfort data. A single-aisle cabin is examined in this study since these remain the most used commercial airplanes,[31] but other configurations may also be explored in the future.

6 | CONCLUSIONS

The current study uses LES simulations to analyze the performance of isothermal opposing-jet airplane cabin mixing ventilation (MV) with time-periodic supply flow rates compared to conventional statistically steady ventilation (SV). The cabin model geometry is comparable with the Airbus A320 or Boeing 737–200 series and incorporates three rows of passengers. Two time-periodic ventilation (TPV) strategies are considered, both employing time-periodic (sinusoidal) supply flow rates (with fixed period and amplitude), but with a phase angle difference between the supply jets depending on the strategy. This results in either an asymmetric forcing of the flow with horizontal oscillating flow patterns (strategy "TPV_AS"), or a symmetric forcing in which high-momentum pulses of the merged jet are generated (strategy "TPV_SS"). The total supply flow rate is constant over time and equal to this of SV. The air exhaled by every passenger (expiratory plumes) is modeled as a statistically steady emission of a passive gas of contaminants. The following conclusions can be drawn:

- TPV supplies fresh air more directly to the passenger zone than SV, either through penetration of the merged jet from above the aisle seat (TPV_AS) or through entrainment of the merged jet flow during pulsations (TPV_SS). Also, the vortices that develop below the lateral inlets under TPV contribute in this respect.
- TPV induces overall higher mean velocities compared to SV. The increase of the volume-averaged velocity amounts up to 55% (TPV_AS) or 43% (TPV_SS) in the passenger zone. Under both SV and TPV, volume-averaged mean velocity levels decrease from the aisle seat zone toward the window seat zone.
- TPV reduces the volume-averaged mean contaminant concentrations in the passenger zone with up to 23% (both TPV cases). This is at the expense of increased concentrations in the surrounding zones (+2% to 8%). The lowest and highest concentrations are observed for the window and middle seat zones (SV), the aisle and middle seat zones (TPV_AS), and the window and aisle seat zones (TPV_SS), respectively. Furthermore, an improved extraction of contaminants from the cabin is realized under TPV.
- The mean penetration of exhaled air concentrations to the passengers in front strongly reduces as a result of an increased perturbation of the expiratory plumes by the TPV flow patterns.
- The mean convective mass transport dominates over turbulent mass transport in most of the cabin (the latter encompassing the random/turbulent fluctuations in case SV, and the turbulent and time-periodic fluctuations in the TPV cases). Using TPV increases both the convective and turbulent mass fluxes in the vertical midplane, for example, in the vicinity of the expiratory plumes, while the longitudinal flux component within the plumes strongly reduces.
- TPV increases the CRE by 20% (TPV_AS) and 9% (TPV_SS) with respect to SV, considering the full cabin volume. In the passenger zone, the increase amounts 28% (TPV_AS) and 23% (TPV_SS). In addition, the ACE increases by 7% in TPV_AS, but slightly decreases (−4%) in TPV_SS. However, in the latter case, the local air change index indicates that a more efficient delivery of fresh air to the passenger zone is realized as well compared with SV.

ACKNOWLEDGMENTS

The Research Foundation – Flanders (FWO) is gratefully acknowledged for their financial support of the PhD fellowship of Jo-Hendrik Thysen (project FWO 1150617N). Special thanks go to Fabio Malizia for his valuable contributions to the numerical simulations, and to Thijs van Druenen for helping with the 3D model of the passenger. This work was carried out on the Dutch national e-infrastructure with the support of SURF Cooperative (projects EINF-1581 and EINF-1938). The partnership with ANSYS CFD is also gratefully acknowledged.

CONFLICT OF INTEREST

The authors have no conflict of interest to declare.

DATA AVAILABILITY STATEMENT

The data that support the findings of this study are available from the corresponding author upon reasonable request.

ORCID

Jo-Hendrik Thysen https://orcid.org/0000-0002-8440-5472
Twan van Hooff https://orcid.org/0000-0002-7811-2745
Bert Blocken https://orcid.org/0000-0003-2935-9562

REFERENCES

1. National Research Council (US). *Committee on Air Quality in Passenger Cabins of Commercial Aircraft, the Airliner Cabin Environment and the Health of Passengers and Crew*. National Academy Press (US); 2002:344.
2. ASHRAE Handbook: Heating, Ventilating, and Air-Conditioning Applications, Inch-Pound Edition, American Society of Heating, Refrigerating and air-Conditioning Engineers (ASHRAE), Atlanta, GA; 2019.
3. Bielecki M, Patel D, Hinkelbein J, et al. Air travel and COVID-19 prevention in the pandemic and peri-pandemic period: a narrative review. *Travel Med Infect Dis*. 2021;39:101915.
4. Elmaghraby HA, Chiang YW, Aliabadi AA. Ventilation strategies and air quality management in passenger aircraft cabins: a review of experimental approaches and numerical simulations. *Sci Technol Built Environ*. 2018;24:160-175.
5. National Research Council (US). *Committee on Airliner Cabin Air Quality, the Airliner Cabin Environment: Air Quality and Safety*. National Academy Press (US); 1986:320.
6. Hocking MB. Passenger aircraft cabin air quality: trends, effects, societal costs, proposals. *Chemosphere*. 2000;41:603-615.
7. Herzog J. Electrification of the environmental control system, 25th International Congress of the Aeronautical Sciences (ICAS), Hamburg, Germany, 3 Sep 2006–8 Sep 2006.
8. Pang L, Xu J, Fang L, Gong M, Zhang H, Zhang Y. Evaluation of an improved air distribution system for aircraft cabin. *Build Environ*. 2013;59:145-152.
9. Singh A, Hosni MH, Horstman RH. Numerical simulation of airflow in an aircraft cabin section. *ASHRAE Trans*. 2002;108(1005):13.
10. Mo H, Hosni MH, Jones BW. Application of particle image velocimetry for the measurement of the airflow characteristics in an aircraft cabin. *ASHRAE Trans*. 2003;109:101-110.
11. Baker AJ, Ericson SC, Orzechowski JA, Wong KL, Garner RP. *Validation for CFD Prediction of Mass Transport in an Aircraft Passenger Cabin, Aerospace Medicine Technical Reports DOT/FAA/AM-06/27*. Office of Aerospace Medicine, Federal Aviation Administration; 2004.

12. Lin CH, Horstman RH, Ahlers MF, et al. Numerical simulation of airflow and airborne pathogen transport in aircraft cabins – part I: numerical simulation of the flow field. *ASHRAE Trans*. 2005;111:755-763.
13. Wang A, Zhang Y, Sun Y, Wang X. Experimental study of ventilation effectiveness and air velocity distribution in an aircraft cabin mockup. *Build Environ*. 2008;43:337-343.
14. Kühn M, Bosbach J, Wagner C. Experimental parametric study of forced and mixed convection in a passenger aircraft cabin mock-up. *Build Environ*. 2009;44:961-970.
15. Zhang Z, Chen X, Mazumdar S, Zhang T, Chen Q. Experimental and numerical investigation of airflow and contaminant transport in an airliner cabin mock up. *Build Environ*. 2009;44:85-94.
16. Liu W, Wen J, Chao J, et al. Accurate and high-resolution boundary conditions and flow fields in the first-class cabin of an MD-82 commercial airliner. *Atmos Environ*. 2012;56:33-44.
17. Giaconia C, Orioli A, Gangi AD. Air quality and relative humidity in commercial aircrafts: an experimental investigation on short-haul domestic flights. *Build Environ*. 2013;67:69-81.
18. Liu W, Wen J, Lin CH, Liu J, Long Z, Chen Q. Evaluation of various categories of turbulence models for predicting air distribution in an airliner cabin. *Build Environ*. 2013;65:118-131.
19. Cao X, Liu J, Pei J, Zhang Y, Li J, Zhu X. 2D-PIV measurement of aircraft cabin air distribution with a high spatial resolution. *Build Environ*. 2014;82:9-19.
20. Li F, Li B, Liu J. Measuring and containing longitudinal flow: important for airborne pollutants control in an aircraft cabin. *Sci Technol Built Environ*. 2015;21:1126-1133.
21. Li J, Cao X, Liu J, Wang C, Zhang Y. Global airflow field distribution in a cabin mock-up measured via large-scale 2D-PIV. *Build Environ*. 2015;93:234-244.
22. Li J, Liu J, Cao X, Jiang N. Experimental study of transient air distribution of a jet collision region in an aircraft cabin mock-up. *Energ Buildings*. 2016;127:786-793.
23. Yang C, Zhang X, Yao Z, Cao X, Liu J, He F. Numerical study of the instantaneous flow fields by large eddy simulation and stability analysis in a single aisle cabin model. *Build Environ*. 2016;96:1-11.
24. Chen W, Liu J, Li F, et al. Ventilation similarity of an aircraft cabin mockup with a real MD-82 commercial airliner. *Build Environ*. 2017;111:80-90.
25. Li J, Liu J, Wang C, Wesseling M, Müller D. PIV experimental study of the large-scale dynamic airflow structures in an aircraft cabin: swing and oscillation. *Build Environ*. 2017;125:180-191.
26. Wang C, Liu J, Li J, Guo Y, Jiang N. Turbulence characterization of instantaneous airflow in an aisle of an aircraft cabin mockup. *Build Environ*. 2017;116:207-217.
27. Zhang Y, Liu J, Pei J, Li J, Wang C. Performance evaluation of different air distribution systems in an aircraft cabin mockup. *Aerosp Sci Technol*. 2017;70:359-366.
28. Zhang Y, Li J, Liu J. Experimental study of the impact of passenger behavior on the aircraft cabin environment. *Sci Technol Built Environ*. 2021;27:427-435.
29. Zhang Y, Li J, Liu M, Liu J, Wang C. Experimental investigation of large-scale flow structures in an aircraft cabin mock-up. *Build Environ*. 2020;184:107224.
30. Mboreha CA, Tytelman X, Nwaokocha C, Layeni A, Okeze RC, Amiri AS. Numerical simulations of the flow fields and temperature distribution in a section of a Boeing 767-300 aircraft cabin. *Mater Today Proc*. 2021;47:4098-4106.
31. Wang C, Zhang J, Chao J, Yang C, Chen H. Evaluation of dynamic airflow structures in a single-aisle aircraft cabin mockup based on numerical simulation. *Indoor Built Environ*. 2022;31(2):398-413.
32. Yu N, Zhang Y, Zhang M, Li H. Thermal condition and air quality investigation in commercial airliner cabins. *Sustainability*. 2021;13:7047.
33. Mazumdar S, Chen Q. Influence of cabin conditions on placement and response of contaminant detection sensors in a commercial aircraft. *J Environ Monit*. 2008;10:71-81.
34. Yan W, Zhang Y, Sun Y, Li D. Experimental and CFD study of unsteady airborne pollutant transport within an aircraft cabin mock-up. *Build Environ*. 2009;44:34-43.
35. Zhang T, Li P, Zhao Y, Wang S. Various air distribution modes on commercial airplanes. Part 1: experimental measurement. *HVAC&R Res*. 2013;19:268-282.
36. Li M, Zhao B, Tu J, Yan Y. Study on the carbon dioxide lockup phenomenon in aircraft cabin by computational fluid dynamics. *Build Simul*. 2015;8:431-441.
37. He J, Yin Y, Yang X, et al. Carbon dioxide in passenger cabins: spatial temporal characteristics and 30-year trends. *Indoor Air*. 2021;31:2200-2212.
38. Lin CH, Horstman RH, Ahlers MF, et al. Numerical simulation of airflow and airborne pathogen transport in aircraft cabins – part II: numerical simulation of airborne pathogen transport. *ASHRAE Trans*. 2005;111:764-768.
39. Sze To GN, Wan MP, Chao CYH, Fang L, Melikov A. Experimental study of dispersion and deposition of expiratory aerosols in aircraft cabins and impact on infectious disease transmission. *Aerosol Sci Tech*. 2009;43:466-485.
40. Wan MP, Sze To GN, Chao CYH, Fang L, Melikov A. Modeling the fate of expiratory aerosols and the associated infection risk in an aircraft cabin environment. *Aerosol Sci Tech*. 2009;43:322-343.
41. Gupta JK, Lin CH, Chen Q. Transport of expiratory droplets in an aircraft cabin. *Indoor Air*. 2011;21:3-11.
42. Silcott D, Kinahan S, Santarpia J, et al. *TRANSCOM/AMC Commercial Aircraft Cabin Aerosol Dispersion Tests*. National Strategic Research Institute; 2020.
43. Yan Y, Li X, Yang L, Yan P, Tu J. Evaluation of cough-jet effects on the transport characteristics of respiratory-induced contaminants in airline passengers' local environments. *Build Environ*. 2020;183:107206.
44. Li X, Zhang T, Fan M, Liu M, et al. Experimental evaluation of particle exposure at different seats in a single-aisle aircraft cabin. *Build Environ*. 2021;202:108049.
45. Yan Y, Li X, Fang X, Yan P, Tu J. Transmission of COVID-19 virus by cough-induced particles in an airliner cabin section. *Eng Appl Com Fluid*. 2021;15:934-950.
46. Fišer J, Jícha M. Impact of air distribution system on quality of ventilation in small aircraft cabin. *Build Environ*. 2013;69:171-182.
47. Pang L, Li P, Bai L, Liu D, Zhou Y, Yao J. Optimization of air distribution mode coupled interior design for civil aircraft cabin. *Build Environ*. 2018;134:131-145.
48. Bosbach J, Lange S, Dehne T, Lauenroth G, Hesselbach F, Allzeit M. Alternative ventilation concepts for aircraft cabins. *CEAS Aeronaut J*. 2013;4:301-313.
49. Liu S, Xu L, Chao J, et al. Thermal environment around passengers in an aircraft cabin. *HVAC&R Res*. 2013;19:627-634.
50. Dehne T. Transient temperature fields of turbulent mixed convection in an aircraft cabin caused by a local heat source. In: Dillmann A, ed. *New Results in Numerical and Experimental Fluid Mechanics X*. Springer; 2014:371-381.
51. Dechow M. Aircraft environmental control systems. In: Hocking MB, ed. *The Handbook of Environmental Chemistry Vol 4H: Air Quality in Airplane Cabins and Similar Enclosed Spaces*. Springer; 2005:3-24.
52. Zhang T, Chen Q. Novel air distribution systems for commercial aircraft cabins. *Build Environ*. 2007;42:1675-1684.
53. Li B, Duan R, Li J, et al. Experimental studies of thermal environment and contaminant transport in a commercial aircraft cabin with gaspers on. *Indoor Air*. 2016;26:806-819.
54. Mundt M, Mathisen HM, Nielsen PV, Moser A. *Ventilation Effectiveness: Rehva Guidebooks*. Federation of European Heating and Air-conditioning Associations; 2004.

55. Hunt HE, Space DR. The Airplane Cabin Environment: Issues Pertaining to Flight Attendant Comfort; 1994
56. Leder K, Newman D. Respiratory infections during air travel. *Intern Med J*. 2005;35:50-55.
57. Cao X, Li J, Liu J, Yang W. 2D-PIV measurement of isothermal air jets from a multi-slot diffuser in aircraft cabin environment. *Build Environ*. 2016;99:44-58.
58. Maier J, Claudia M-M, Zinn F, Dehne T, Bosbach J. Ceiling-based cabin displacement ventilation in an aircraft passenger cabin: analysis of thermal comfort. *Build Environ*. 2018;146:29-36.
59. Bosbach J, Heider A, Dehne T, Markwart M, Gores I, Bendfeldt P. Evaluation of cabin displacement ventilation under flight conditions. 28th International Congress of the Aeronautical Sciences (ICAS2012), Sept. 2012, Brisbane, Australia
60. Liu M, Chang D, Liu J, et al. Experimental investigation of air distribution in an airliner cabin mockup with displacement ventilation. *Build Environ*. 2021;191:107577.
61. Maier J, Marggraf-Micheel C, Dehne T, Bosbach J. Thermal comfort of different displacement ventilation systems in an aircraft passenger cabin. *Build Environ*. 2017;111:256-264.
62. Zhang T, Yin S, Wang S. An under-aisle air distribution system facilitating humidification of commercial aircraft cabins. *Build Environ*. 2010;45:907-915.
63. Shi Z, Bai J, Han Y. Distribution of ozone and its volatiles in indoor environment: a numerical simulation with CFD for the aircraft cabin. *Environ Technol*. 2020;41:3146-3156.
64. American Society of Heating, Refrigerating and Air-Conditioning Engineers. *ANSI/ASHRAE standard 161–2018: Air Quality within Commercial Aircraft*. ASHRAE; 2018.
65. You R, Chen J, Lin CH, Wei D, Chen Q. Investigating the impact of gaspers on cabin air quality in commercial airliners with a hybrid turbulence model. *Build Environ*. 2017;111:110-122.
66. Li J, Cao X, Mohanarangam K, Yang W. PIV measurement of human thermal convection flow in a simplified vehicle cabin. *Build Environ*. 2018;144:305-315.
67. Walkinshaw DS. A brief introduction to passenger aircraft cabin air quality. *ASHRAE J*. 2020;62:12-18.
68. Wang C, Xu J, Fu SC, Chan KC, Chao CYH. Respiratory bioaerosol deposition from a cough and recovery of viable viruses on nearby seats in a cabin environment. *Indoor Air*. 2021;31:1913-1925.
69. Dygert RK, Dang TQ. Mitigation of cross-contamination in an aircraft cabin via localized exhaust. *Build Environ*. 2010;45:2015-2026.
70. Zitek P, Vyhlídal T, Simeunivić G, Nováková L, Čížek J. Novel personalized and humidified air supply for airliner passengers. *Build Environ*. 2010;45:2345-2353.
71. Melikov AK, Dzhartov V. Advanced air distribution for minimizing airborne cross-infection in aircraft cabins. *HVAC&R Res*. 2013;19:926-933.
72. You R, Zhang Y, Zhao X, et al. An innovative personalized displacement ventilation system for airliner cabins. *Build Environ*. 2018;137:41-50.
73. You R, Lin CH, Wei D, Chen Q. Evaluating the commercial airliner cabin environment with different air distribution systems. *Indoor Air*. 2019;29:840-853.
74. Wu C, Ahmed NA. Numerical study of transient aircraft cabin flowfield with unsteady air supply. *J Aircr*. 2011;48:1984-2001.
75. Wu C, Na A. A novel mode of air supply for aircraft cabin ventilation. *Build Environ*. 2012;56:47-56.
76. Kandzia C, Schmidt M, Müller D. Room airflow effects applying unsteady boundary conditions. The 12th International Conference on Air Distribution in Rooms (Roomvent 2011), Jun 2011, Trandheim, Norway.
77. Schmidt M, Kandzia C, Mueller D. Instationary operation of a ventilation system. 34th AIVC Conference, Sept 2013, Athens, Greece.
78. van Hooff T, Blocken B. Mixing ventilation driven by two oppositely located supply jets with a time-periodic supply velocity: a numerical analysis using computational fluid dynamics. *Indoor Built Environ*. 2020;29(4):603-620.
79. Thysen J-H, van Hooff T, Blocken B, van Heijst GJF. Numerical study of time-periodic mixing ventilation: effect of amplitude. Healthy Buildings Europe, Jul 2017, Lublin, Poland.
80. ANSYS, Inc. SpaceClaim Documentation, Release 2020 R2. Published: 19 Sept. 2020.
81. AIRBUS A320. Aircraft characteristics, airport and maintenance planning. Technical report, Issue Sep 30/85 Rev December 2020, AIRBUS S.A.S, France.
82. BOEING, 737 Airplane characteristics for airport planning. Technical report, nr. D6-58325-6, Rev A September 2020, Boeing Commercial Airplanes, USA.
83. Quigley C, Southall D, Freer M, Moody A, Porter M. *Anthropometric Study to Update Minimum Aircraft Seating Standards. Report Prepared for Joint Aviation Authorities*. ICE Ergonomics Ltd.; 2001.
84. Autodesk Meshmixer, version 3.5.474, Manual 2017.
85. ANSYS, Inc. ANSYS Fluent Theory Guide, Release 2020 R2.
86. Pope SB. *Turbulent Flows*. Cambridge University Press; 2000.
87. Sørenson DN, Voigt LK. Modelling flow and heat transfer around a seated human body by computational fluid dynamics. *Build Environ*. 2003;38:753-762.
88. Hefny M, Ooka R. Influence of cell geometry and mesh resolution on large eddy simulation predictions of flow around a single building. *Build Simul*. 2008;1:251-260.
89. Duan R, Liu W, Xu L, et al. Mesh type and number for CFD simulations of air distribution in an aircraft cabin. *Numer Heat Transf B Fundam*. 2015;67(6):489-506.
90. Blocken B. Computational fluid dynamics for urban physics: importance, scales, possibilities, limitations and ten tips and tricks towards accurate and reliable simulations. *Build Environ*. 2015;91:219-245.
91. ANSYS, Inc. ANSYS Fluent User's Guide, Release 2020 R2.
92. Afgan I, Moulinec C, Laurence D. Numerical simulation of generic side mirror of a car using large eddy simulation with polyhedral meshes. *Int J Numer Meth Fluids*. 2008;56:1107-1113.
93. Spiegel M, Redel T, Zhang J, et al. Tetrahedral vs. polyhedral mesh size evaluation on flow velocity and wall shear stress for cerebral hemodynamic simulation. *Comput Method Biome*. 2011;14(1):9-22.
94. Chen H, Zhou X, Feng Z, Cao SJ. Applicatin of polyhedral meshing strategy in indoor environment simulation: model accuracy and computing time. *Indoor Built Environ*. 2021;31:719-731.
95. Zhang T, Li P, Zhao Y, Wang S. Various air distribution modes on commercial airplanes – part 2: computational fluid dynamics modeling and validation. *HVAC&R Res*. 2013;19:457-470.
96. Mathey F, Cokljat D, Bertoglio JP, Sergent E. Assessment of the vortex method for large eddy simulation inlet conditions. *Prog Comput Fluid Dyn*. 2006;6:58-67.
97. Thysen J-H, van Hooff T, Blocken B, van Heijst GJF. CFD simulations of two opposing plane wall jets in a generic empty airplane cabin: comparison of RANS and LES. *Build Environ*. 2021;205:108174.
98. Gao N, Niu J. CFD study on micro-environment around human body and personalized ventilation. *Build Environ*. 2004;39(7):795-805.
99. Yakhot V, Orszag SA, Thangam S, Gatski TB, Speziale CG. Development of turbulence models for shear flows by a double expansion technique. *Phys Fluids A*. 1992;4:1510-1520.
100. Gerasimov A. *Quick Guide to Setting up LES-Type Simulations, Version 1.4*. European Technology Group, ANSYS Sweden AB; 2016.
101. Kim WW, Menon S. Application of the Localized Dynamic Subgrid-Scale Model to Turbulent Wall-Bounded Flows, Technical Report AIAA-97-0210, 35th Aerospace Science Meeting, American Institute of Aeronautics and Astronautics, Reno, NV, USA; 1997.

102. Wang M, Chen Q. Assessment of various turbulence models for transitional flows in an enclosed environment. *HVAC&R Res*. 2009;15(6):1099-1119.
103. Franke J, Hellsten A, Schlünzen H, Carissimo B. (Eds.). Best practice guideline for the CFD simulation of flows in the urban environment. COST Office Brussels, ISBN 3–00–018312-4; 2007.
104. Blocken B, Carmeliet J. Pedestrian wind conditions at outdoor platforms in a high-rise apartment building: generic sub-configuration validation, wind comfort assessment and uncertainty issues. *Wind Struct*. 2008;11(1):51-70.
105. Blocken B, Janssen WD, van Hooff T. CFD simulation for pedestrian wind comfort and wind safety in urban areas: general decision framework and case study for the Eindhoven University campus. *Environ Modell Softw*. 2012;30:15-34.
106. Liddament M. A review of ventilation efficiency. Technical Note AIVC 39. International Energy Agency, Air infiltration and Ventilation Centre; 1993.
107. Etheridge DW, Sandberg M. *Building Ventilation: Theory and Measurement*. John Wiley & Sons; 1996.
108. Zou X, Ouyang Q, Lin G, Zhu Y. Impact of dynamic airflow on human thermal response. *Indoor Air*. 2006;16:348-355.
109. Huang L, Ouyang Q, Zhu Y. Perceptible airflow fluctuation frequency and human thermal response. *Build Environ*. 2012;54:14-19.
110. Luo M, Yu J, Ouyang Q, Cao B, Zhu Y. Application of dynamic airflows in buildings and its effects on perceived thermal comfort. *Indoor Built Environ*. 2018;27:1162-1174.
111. Buonocore C, Vecchi RD, Lamberts R, Güths S. From characterisation to evaluation: a review of dynamic and non-uniform airflows in thermal comfort studies. *Build Environ*. 2021;206:108386.
112. Körner M, Resagk C, Thess A. Rayleigh number dependence of the Archimedes number dependent large-scale flow structure formation in mixed convection, 15th European Turbulence Conference, Delft, the Netherlands, 25 Aug 2015–28 Aug 2015.
113. Kandzia C, Mueller D. Flow structures and Reynolds number effects in a simplified ventilated room experiment. *Int J Vent*. 2016;15(1):31-44.
114. Kandzia C, Mueller D. Stability of large room airflow structures in a ventilated room. *Int J Vent*. 2018;17(1):1-16.
115. Gousseau P, Blocken B, van Heijst GJF. CFD simulation of pollutant dispersion around isolated buildings: on the role of convective and turbulent mass fluxes in the prediction accuracy. *J Hazard Mater*. 2011;194:422-434.
116. van Hooff T, Blocken B, Gousseau P, van Heijst GJF. Counter-gradient diffusion in a slot-ventilated enclosure assessed by LES and RANS. *Comput Fluids*. 2014;96:63-75.
117. Liu W, You R, Zhang J, Chen Q. Development of a fast fluid dynamics-based adjoint method for the inverse design of indoor environments. *J Build Perform Simul*. 2017;10:326-343.
118. Li N, Yang L, Li X, Li X, Tu J, Cheung S. Multi-objective optimization for designing of high-speed train cabin ventilation system using particle swarm optimization and multi-fidelity kriging. *Build Environ*. 2019;155:161-174.

SUPPORTING INFORMATION

Additional supporting information can be found online in the Supporting Information section at the end of this article.

How to cite this article: Thysen J-H, van Hooff T, Blocken B, van Heijst G. Airplane cabin mixing ventilation with time-periodic supply: Contaminant mass fluxes and ventilation efficiency. *Indoor Air*. 2022;32:e13151. doi: 10.1111/ina.13151

APPENDIX A

Figure A1 visualizes the zones in which the longitudinal mean convective mass flux $Q_{c,z}$ is at least an order of magnitude smaller than the two other mean convective mass flux components $Q_{c,x}$ and $Q_{c,y}$ (black color; "zone *XY*"), or has equal or larger magnitude compared to $Q_{c,x}$ and $Q_{c,y}$ (white color; "zone *Z*"), with values in between indicated by the gray color (zone "*XYZ*"), based on the ratios $|Q_{c,z}/Q_{c,x}|$ and $|Q_{c,z}/Q_{c,y}|$ obtained at every grid cell and subjected to the following conditions:

- Zone *XY* (black color): $|Q_{c,z}/Q_{c,x}| \leq 0.1$ *or* $|Q_{c,z}/Q_{c,y}| \leq 0.1$
- Zone *XYZ* (gray color): $|Q_{c,z}/Q_{c,x}| > 0.1$ *and* $|Q_{c,z}/Q_{c,y}| > 0.1$ *and* with at least one of the two ratios in between 0.1 and 1
- Zone Z (white color): $|Q_{c,z}/Q_{c,x}| \geq 1$ *and* $|Q_{c,z}/Q_{c,y}| \geq 1$

In the vertical midplane (Figure A1a), in all ventilation cases, the majority of data points (50–52%) is in zone *XY* (black color) and only a minority (6%–8%) is in zone *Z* (white color). In the horizontal plane (Figure A1b), most of the data points (52%–58%) are in zone *XYZ* (gray color), and about 28% (SV) or 22%–23% (TPV) of the data points have significant longitudinal flow (zone *Z*; white color). Overall, considering the data points in both planes, with most of the points being in zones *XYZ* (47%–50%) and *XY* (35%–38%), the convective flux in the longitudinal direction is secondary compared to the two other convective flux components. Further analyses indicate that about 72%–75% of the points in zone *XYZ* (both planes) are characterized by $|Q_{c,z}/Q_{c,x}|$ or $|Q_{c,z}/Q_{c,y}|$ lower than 0.5.

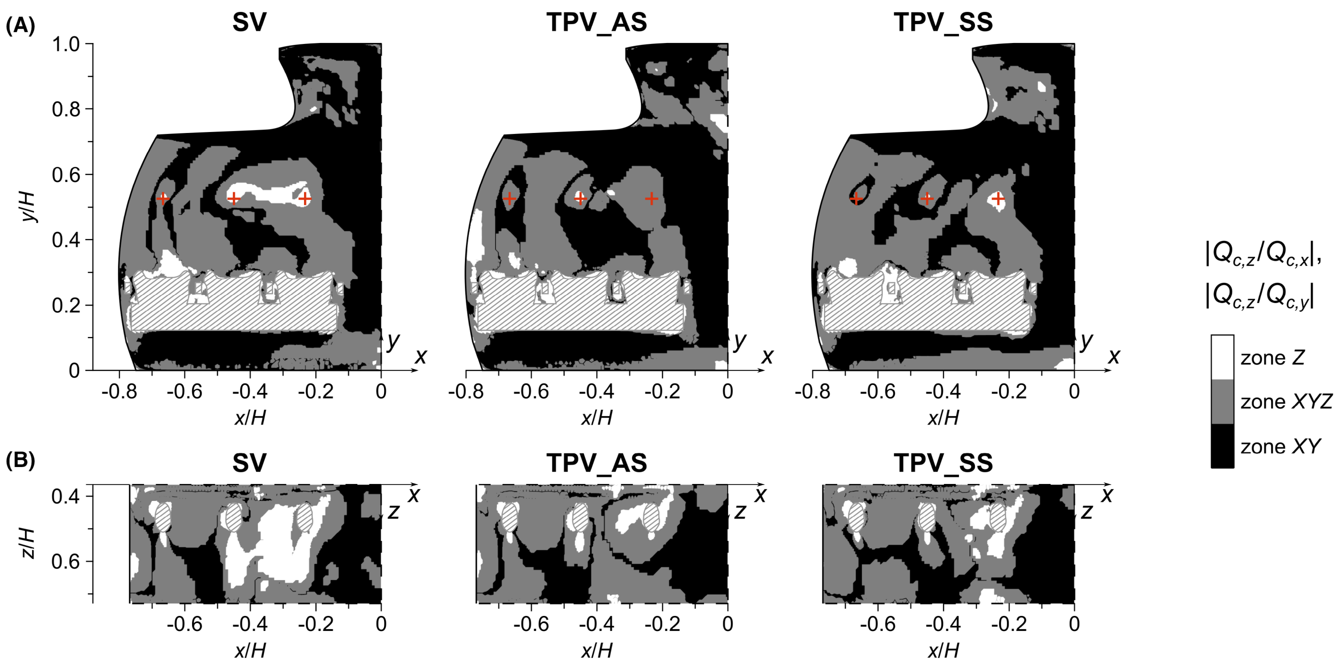

FIGURE A1 Relative magnitude of longitudinal mean convective mass flux ($Q_{c,z}$) compared with other mean convective mass flux components ($Q_{c,x}$ and $Q_{c,y}$) for SV (left), TPV_AS (middle) and TPV_SS (right), in (A) vertical midplane ($z/H \approx 0.55$) and (B) horizontal plane ($y/H \approx 0.53$), visualized as zones *Z*, *XYZ*, and *XY* according to conditions specified in text. The red plus symbols in (A) indicate source locations (mouth) at $x/H \approx -0.23$, -0.45, and -0.67.

APPENDIX B

The two turbulent flux components $Q_{t,i}/Q_{ref}$ presented in Figure 11A,B for case SV are reproduced in Figure B1, but the (dotted) isoline of zero mean concentration gradient along the corresponding direction x_i (i.e. $\partial C/\partial x_i = 0$) is added. The sign of $\partial C/\partial x_i$ is also shown in the circles. The isoline intersects the source locations, with at both sides $Q_{t,i}$ and the gradient having an opposite sign, confirming that the turbulent mass transport occurs from high to low concentrations (diffusion mechanism). On the contrary, counter-gradient areas ($\partial C/\partial x_i$ and $Q_{t,i}$ have same sign) are also predicted, for example, below the lateral supply jet in Figure B1A at $x/H \approx -0.3$. In such areas, the standard gradient-diffusion assumption ($Q_{t,i} = -D_t \partial C/\partial x_i$, with D_t the turbulent mass diffusivity), often used in RANS simulations, is invalid. This may contribute to an erroneous RANS prediction of the concentration distribution in case the turbulent mass transport is significant compared to convection, which — in the current study — is not, as illustrated in Figure 12. Similar results are found for the TPV cases (not shown).

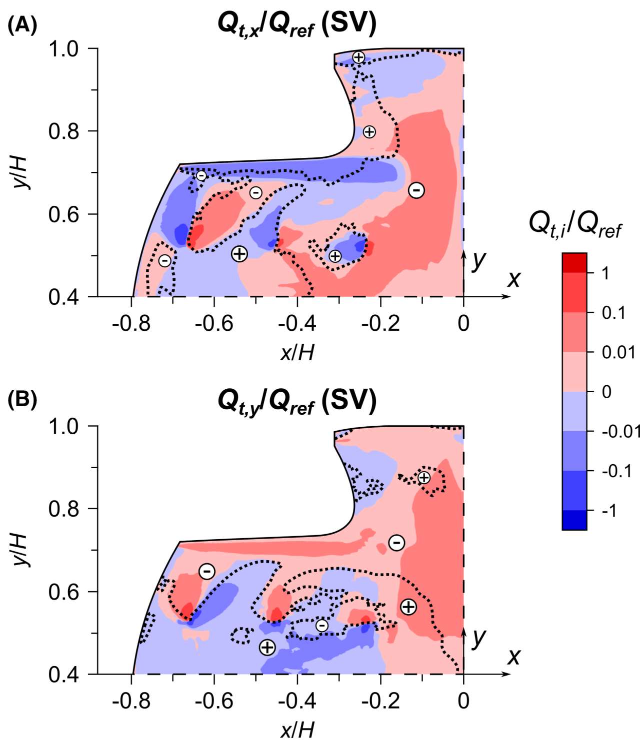

FIGURE B1 Contours of mean turbulent mass flux components ($Q_{t,i}/Q_{ref}$) in vertical midplane ($z/H \approx 0.55$) obtained with LES for SV (see also Figure 11A,B), with (dotted) isoline of zero mean concentration gradient in corresponding direction ($\partial C/\partial x_i = 0$) and indication of sign of $\partial C/\partial x_i$ in circles: (a) $Q_{t,x}/Q_{ref}$ and $\partial C/\partial x$; (b) $Q_{t,y}/Q_{ref}$ and $\partial C/\partial y$.